Summer 8-7-2018

Indirect Imaging using Heterodyne Remote Digital Holography

Muralidhar Madabhushi Balaji
Southern Methodist University, mmadabhushibalaji@smu.edu

INDIRECT IMAGING USING HETERODYNE REMOTE DIGITAL HOLOGRAPHY

Approved by:

_____

Dr. Marc Christensen
Professor of Electrical Engineering

_____

Dr. Duncan MacFarlane
Professor of Electrical Engineering

_____

Dr. Oliver Cossairt
Associate Professor

_____

Dr. Prasanna Rangarajan
Assistant Professor

IMAGING OBJECTS HIDDEN FROM VIEW USING HETERODYNE REMOTE DIGITAL HOLOGRAPHY

A Thesis Presented to the Graduate Faculty of the

Bobby B. Lyle school of Engineering

Southern Methodist University

in

Partial Fulfillment of the Requirements

for the degree of

Master of Science in Electrical Engineering

by

Muralidhar Madabhushi Balaji

B.Tech., Electronics and Instrumentation Engineering, JNTU, Hyderabad, India, 2014

August 07, 2018

ACKNOWLEDGMENTS

I would like to thank my advisors Prof. Marc Christensen and Dr. Prasanna Rangarajan for providing me with this wonderful opportunity to work on OMNISCIENT project. I would like to thank Prof. Duncan Macfarlane for his valuable guidance and critical feedback. I thank Prof. Oliver Cossairt for serving on my committee and providing valuable feedback on my work. I am greatly indebted to Prasanna for the enormous amounts of time and effort he had spent in shaping me over the past two years. I am also grateful to Dr. Indranil Sinharoy for all his support and continued guidance. I also thank Andreas Corliano, from Heliotis for all the technical support he had provided for using the lock-in camera.

I would like to thank Dr.Sai Siva Gorthi for introducing me to the field of optical metrology by giving me an opportunity to work in OMI lab, IISc. I would also like to thank my colleagues at OMI lab for all the valuable discussions and suggestions during my time there. I am forever indebted to Prof.Akshay from my undergrad. He is a constant source of motivation and had always encouraged me in all my professional endeavors.

A great deal of acknowledgement goes to my colleague and best friend Aparna Viswanath. She has helped me in numerous ways in my professional endeavors during the last two years and I can't thank her enough for all the help. I would also like to thank my colleagues Ashwini and Brian. I would like to thank Lorna, Becky, Elizabeth, Susan, Danielle and Julie for all the help they have provided over the course of last two years.

I am grateful to all my roommates in the US, Aakash, Dhaval, Vivek and Dhruvang for being so understanding and supportive. I would also like to thank my friends Anna, Nathan and Lakshmi. And to Anu, Siva, Vamshi, Sashi, Bharat and Surya, I am lucky to have found friends like you guys.

And finally, I would forever be grateful to Amma, Appa, Tatha and Pati. If not for your unwavering trust and support, I would have never achieved whatever little I have achieved. And, miss you Brownie.

Madabhushi Balaji, Muralidhar B.Tech., Electronics and Instrumentation, JNTU

Imaging objects hidden from view using heterodyne remote digital holography

Advisor: Dr. Marc Christensen
Master of Science degree conferred on August 7th 2018
Thesis completed on August 6th 2018

Conventional line-of-sight imaging techniques rely on detecting light paths bouncing from the object and reaching directly to the detector. Absence of any such direct light paths from object to detector results in a failure to recover any useful information using conventional techniques. The absence of direct light paths from object to detector can be observed in several real-world scenarios such as looking around a corner, imaging through turbid media, imaging through tissue etc.

The focus of this thesis is pertaining to the problem of looking around corners (or) imaging object hidden from line of sight at macroscopic scales. This thesis focuses on adapting heterodyne interferometry to circumvent the radiometry losses due to scattering and thereby enabling its use in more challenging practical scenarios. Objects hidden around a corner were reconstructed with 500 μm resolution at 0.8 meters standoff. Using heterodyne interferometry and lock-in detection techniques, the hologram of the hidden object could be obtained even under significant radiometry losses without any power matching. Also discussed is the estimation of rapidly varying and slowly varying motion of objects around a corner using doppler shifts and speckle correlations respectively.

TABLE OF CONTENTS

LIST OF FIGURES

This thesis is dedicated to my Dad*

*I love you too, mom :)

Chapter 1

HETERODYNE INTERFEROMETRY FOR INDIRECT IMAGING

1.1 Motivation

Gleaning information by detecting multi bounce, indirect light paths from object to detector has applications in several real-world scenarios such as imaging around corners, imaging through turbid media and imaging through tissue. Hence, significant interest has been devoted by research groups across the world towards developing techniques to recover information of objects from these indirect light paths. The methods developed span a range of scales from microscopy to macroscopic scales with varying levels of complexity.

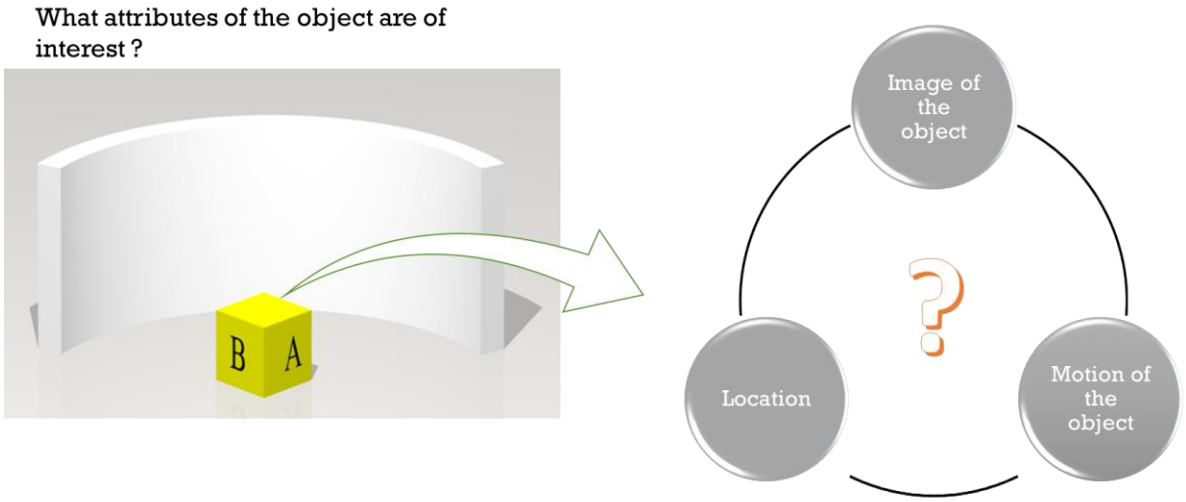

Figure 1-1: Illustration depicting an example scenario of imaging objects hidden from view.

Conventional imaging techniques rely on detecting light paths bouncing from the object and reaching directly to the detector. The absence of any such direct light paths from object to detector results in a failure of recovering useful information of the object using line-of-sight imaging techniques. Indirect imaging encompasses a variety of imaging techniques which address the problem of recovering information in the absence of direct light paths from object to detector.

The focus of this thesis is on imaging objects hidden from the direct line of sight of the imager at macroscopic scales. In the canonical scene illustrated in Figure 1-1 by observing the visible surface S, we would like to infer the characters written on the obscured faces of the box. As with line of sight imaging, where the location, texture and motion of the object can be estimated we explore the possibility of estimating the texture, location and motion of the object hidden from view. We rely on principles of heterodyne interferometry and lock-in detection to extract the object's hologram despite significant radiometric losses caused by scattering at the walls. A brief introduction to holography is presented in Section 1.2, followed by a literature review of the existing indirect imaging methods in Section 1.3. Sections 1.4 and 1.5 discuss the heterodyne interferometry and lock-in detection concepts.

1.2 Holography

Light is complex field with both amplitude and phase. Knowledge of the phase of light at a location in space can be used to infer the phase and amplitude of the field at a different location in space. But, conventional detectors are capable of recording only the intensity of an incident field thereby losing access to the phase information of the field. Holography solves this problem by recording an interference pattern of the object field with a known reference field [1].

Consider the object beam represented by,

$$\mathcal{U}_{object}(\boldsymbol{x}) = A_{object}(\boldsymbol{x}) \exp\left(-i\phi_{object}(\boldsymbol{x})\right) \tag{1-1}$$

And, the reference beam represented by,

$$\mathcal{U}_{reference}(\boldsymbol{x}) = A_{reference}(\boldsymbol{x}) \exp\left(-i\phi_{reference}(\boldsymbol{x})\right) \tag{1-2}$$

The recorded intensity of the interference of the two beams can be represented as,

$$I(\boldsymbol{x}) = \left|\mathcal{U}_{reference}(\boldsymbol{x}) + \mathcal{U}_{object}(\boldsymbol{x})\right|^2 \tag{1-3}$$

$$I(\boldsymbol{x}) = \begin{Bmatrix} \left|A_{reference}(\boldsymbol{x})\right|^2 + \left|A_{object}(\boldsymbol{x})\right|^2 + \\ A_{reference}(\boldsymbol{x})A_{object}(\boldsymbol{x}) \exp\left(-i\left(\phi_{object}(\boldsymbol{x}) - \phi_{reference}(\boldsymbol{x})\right)\right) \\ + A_{reference}(\boldsymbol{x})A_{object}(\boldsymbol{x}) \exp\left(-i\left(\phi_{object}(\boldsymbol{x}) - \phi_{reference}(\boldsymbol{x})\right)\right) \end{Bmatrix} \tag{1-4}$$

It can be observed from Equation (1-4) that the third and the fourth terms of the detected irradiance contains the information of amplitude and the relative phase of the object with respect to reference. By multiplying the hologram term, $A_{reference}(\boldsymbol{x})A_{object}(\boldsymbol{x}) \exp\left(-i\left(\phi_{object}(\boldsymbol{x}) - \phi_{reference}(\boldsymbol{x})\right)\right)$ with the complex conjugate of the reference field, the object field, $A_{object}(\boldsymbol{x}) \exp\left(-i\phi_{object}(\boldsymbol{x})\right)$ can be obtained.

The experiments described in this thesis are done in Fourier transform holography configuration. A brief description of Fourier transform holography is presented in the next section.

1.2.1 Fourier transform holography

In Fourier transform holography [2], the reference beam is a point like source in the vicinity of the object. Thus, the interference patterns recorded on the detector can be considered as a superposition of Young's fringes arising from the pairwise interference of the reference beam with the secondary point sources that make up the object. A simple Fourier transformation of the recorded intensity would result in reconstruction of the object field. Most of the experimental results presented in this thesis were captured using a Fourier transform holographic setup.

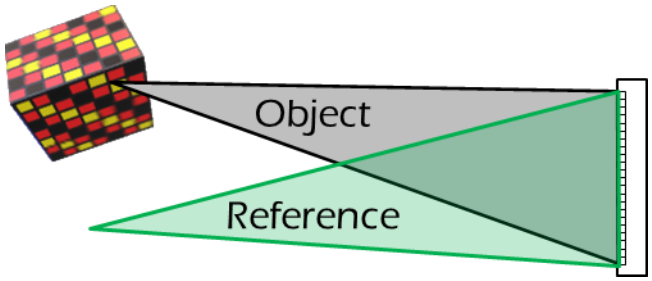

Figure 1-2: Recording of a Fourier transform hologram.

1.2.2 Diffuse illumination holography

In traditional holography, the object is illuminated by a spatially homogeneous beam and the hologram is recorded. But, in the case of looking around corners, the object is illuminated by a scattered field from the wall. Thus, the beam illuminating the object is no longer homogeneous but is speckle due to scattering at the wall. At first glance, although this might appear to be a problem, holography using diffuse illumination is a well-known technique [3]. But, the object can be considered as a collection of points sources interfering with a reference and hence can still be reconstructed except for the fact that the reconstructed object would appear noisy with speckle riding on top. This is also known as diffuse illumination holography.

1.3 Literature review

The existing methods for indirect imaging can be classified based upon the type of illumination source used. This section briefly reviews these methods:

Pulsed Illumination sources:

By measuring the precise round-trip time of flight information of ultra-short light pulses from the wall to object to detector, shapes of objects hidden around a corner can be reconstructed [4,5]. These techniques rely on ultrafast detectors to estimate the timing information of the pulses. From these times of flight measurements, the object shapes are estimated using sophisticated algorithms. The spatial resolution of the reconstructed shapes of objects depends upon the timing resolution of the detectors.

Pulsed illumination sources are also used to time gate the ballistic photons and image objects through scattering media such as biological specimen. These techniques rely on the fact that the light that interacted only with the object within the scattering medium would arrive first. All the multiply scattered light would travel longer distance through the medium and hence can be gated out. This way, by collecting only the photons that interacted with the object, effects of scattering media are mitigated and object image can be reconstructed [6,7].

Continuous Illumination sources:

Phase conjugation techniques using coherent continuous wave sources have applications in focusing light through tissues [10]. In these techniques, the phase perturbation caused by the randomizing medium is first estimated using a guide star. Subsequently, the emerging wave front from the object is passed through a phase conjugating element to negate the perturbing influence of the medium. In focusing through tissues, and ultrasound beam is focused through the medium

to act as a guide star. Multiply scattered light within the media would interact at the region of focus and experiences a doppler shift in its frequency. The scattered light from the ultrasound focus region is holographically recorded and to estimate the phase. A beam with the conjugate phase profile is launched through the medium to create optical focusing.

Techniques relying on an adaptation of imaging correlography for satellite imaging [20] have been used to recover images of objects around corners and to image through turbid media [18,19]. Imaging correlography techniques were originally used to recover satellite images from scattered speckle patterns of the coherently illuminated object. Speckle correlations have been exploited by Eitan *et.al*., to do imaging of objects through turbid media.

Freund *et.al*., have developed an approach relying on the speckle memory effect for imaging around corners [8]. Ori Katz *et.al.,* relied on this principle to reconstruct objects around a corner [9]. In this approach, the hidden object can be considered as a collection of incoherent point sources which produce a superposition of shifted speckle patterns after scattering off the scattering surface. The compact autocorrelation support of the speckle patterns (*autocorrelation of a speckle pattern can be approximated by a Dirac delta function*) is exploited here to reconstruct the hidden object from this speckle pattern. The autocorrelation of the superposition of speckle patterns result in an autocorrelation of the hidden object itself (*due to its convolution with a delta function*). Phase retrieval methods are utilized to recover the intensity image of the object from its autocorrelation.

In holographic methods the object beam is interfered with a reference beam to obtain the hologram of object through scattering medium. For small angular separations, the reference beam conjugates the random phase introduced by the medium to form the hologram of the object. This approach was used to do holographic imaging of objects through scattering medium [11,12]. This

approach has been adapted to perform holographic imaging of object hidden around a corner [13,14].

Of the discussed approaches, holographic approach, time of flight and speckle correlations were used at macroscopic scales to look around corners. But, all these approaches face severe radiometric losses of the order of 120dB in practical scenarios with Lambertian reflecting objects and surfaces [21]. Here, an approach to reconstruct the hidden object even under significant radiometry losses using heterodyne interferometry is presented. The next section introduces the concept of heterodyne interferometry and its applications in recovering weakly reflecting objects.

1.4 Heterodyne Interferometry for recovering weak signals

Heterodyne detection (*also known as coherent detection, phase-sensitive detection*) is widely used in the field of radio communications to detect weak signals buried in noise. This detection methodology relies on the orthogonality of complex sinusoids. It acts as a temporal notch filter by accumulating the signal of interest within the detection bandwidth, thereby reducing the broadband noise and improving the system SNR [23].

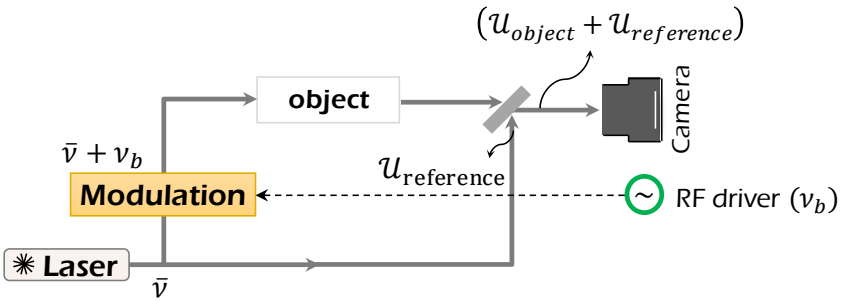

Figure 1-3: Heterodyne Interferometer Schematic.

Optical heterodyne detection relies on the same principle except that the heterodyne signal is generated by two frequency shifted coherent beams interfering on a square law detector (*such as*

a photodiode) [22]. A typical heterodyne interferometer is illustrated in Figure 1-3**.** Two linearly polarized, monochromatic optical beams at temporal frequency $\bar{\nu}\,Hz$ and $\bar{\nu}+\nu_b\,Hz$ interfere on a photodetector. The two beams can be represented as,

$$\mathcal{U}_{object}(\boldsymbol{x},t)=A_{object}(\boldsymbol{x})\exp\left(-i\left(2\pi(\bar{\nu}+\nu_b)t+\ \emptyset_{object}(\boldsymbol{x})\right)\right) \qquad (1\text{-}5)$$

And,

$$\mathcal{U}_{reference}(\boldsymbol{x},t)=A_{reference}(\boldsymbol{x})\exp\left(-i\left(2\pi\bar{\nu}t+\emptyset_{reference}(\boldsymbol{x})\right)\right) \qquad (1\text{-}6)$$

The intensity of the interference of the two beams is represented as,

$$I(\boldsymbol{x},t)$$

$$=\left\{\begin{array}{c}\left|A_{reference}(\boldsymbol{x})\right|^2+\left|A_{object}(\boldsymbol{x})\right|^2+\\ \left|A_{reference}(\boldsymbol{x})\right|\left|A_{object}(\boldsymbol{x})\right|\exp\left(-i\left(2\pi\nu_b t+\emptyset_{reference}(\boldsymbol{x})-\ \emptyset_{object}(\boldsymbol{x})\right)\right)+\\ \left|A_{reference}(\boldsymbol{x})\right|\left|A_{object}(\boldsymbol{x})\right|\exp\left(i\left(2\pi\nu_b t+\ \emptyset_{reference}(\boldsymbol{x})-\ \emptyset_{object}(\boldsymbol{x})\right)\right)\end{array}\right\} \qquad (1\text{-}7)$$

It can be observed from Equation(1-7) that the detected irradiance is comprised of three terms oscillating at three distinct temporal frequencies. The significant advantage offered by the heterodyning process can be observed by noticing the magnitude of the hologram term. The magnitude of the hologram term is a product of the reference beam amplitude and the object beam amplitude $\left|A_{reference}(\boldsymbol{x})\right|\left|A_{object}(\boldsymbol{x})\right|$. Thus, the weak signal contribution from the object can be significantly amplified (*upto shot-noise level of the reference beam*) by having a strong reference beam [23]. It is important to note that the hologram term has to be isolated independant of the other terms as the zeroth order terms can overwhelm the detected irradiance otherwise. The ability to isolate the hologram term independant of the other terms and thereby amplifying a weak signal forms the basis for weak signal recovery using heterodyne interferometry.

Figure 1-4 illustrates the block diagram of lock-in detection system. A photo detector output signal is passed through a lock-in amplifier to perform the lock-in demodulation. The photodetector output is simultaneously multiplied by a sine and cosine waveform at the demodulation frequency in two channels. The output is then low- pass filtered. The low pass filtered output represents the in-phase and quadrature components of the demodulated signal.

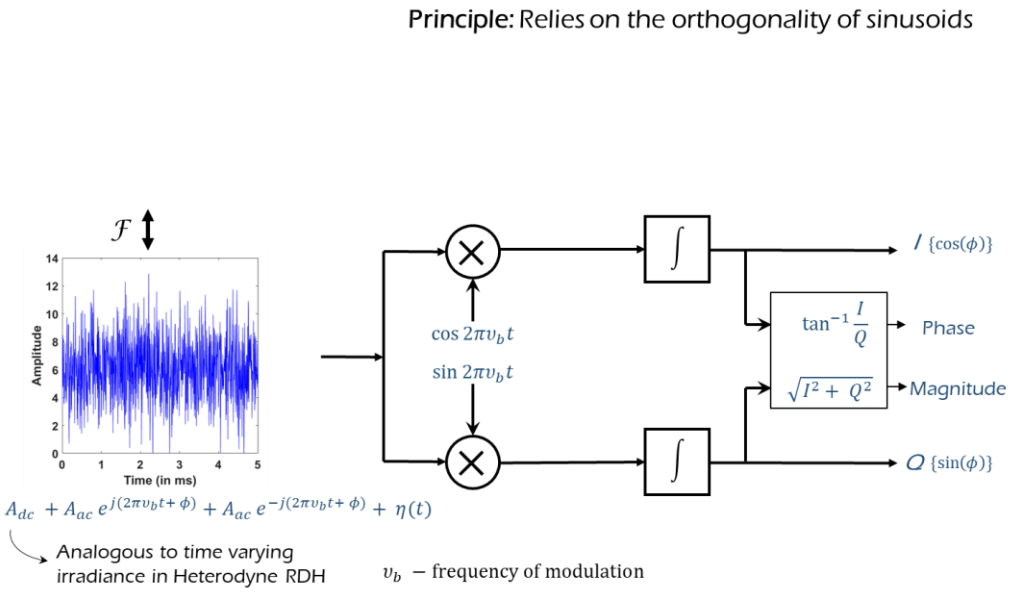

Figure 1-4: Coherent detection schematic.

Heterodyne Interferometry is widely used in several applications where light return from the object is very low [23]. In long distance measurements, such as ranging etc. shot noise limited measurements using heterodyne interferometry were performed [24]. It has also been used in white light interferometry for profiling weakly reflecting objects [25]. Space based heterodyne interferometers are being used to detect very weak gravitational waves as a part of LISA [26]. Heterodyne interferometry is also used in several biological applications for focusing through tissue [27].

Traditionally, lock-in detection has been performed using a single pixel detector followed by a lock-in amplifier. With the availability of high frame rate focal plane arrays, full field lock-in demodulation can be performed by 4-bucket sampling (capturing 4 frames within a period and computationally extracting the amplitude and phase) [30]. But, the disadvantage of these systems is the fact that, in each frame, the signal and the background are simultaneously recorded and thereby limiting the dynamic range available for recording the signal. Advances in interferometry and 3D imaging have furthered the development of focal plane arrays capable of performing pixel level lock-in demodulation. A brief description of the commercially available lock-in camera used in our experiments is presented in the next section.

1.5 Lock-in Camera

The lock-in camera [31] used in the experiments presented in this thesis features a pixel level lock-in demodulation. By having an additional circuitry to compensate for the unmodulated signal from saturating the sensor [32], the lock-in camera can use nearly all its dynamic range in recording the amplitude and phase of the modulated signal. Thus, with this advanced detector, very high heterodyne gain can be achieved, and the signal can be recorded even under large signal to background conditions.

Figure 1-5 illustrates the functioning of the lock-in camera. Demodulation of the time varying irradiance is accomplished at each pixel by using two quadrature bi-polar waveforms that match the temporal frequency of the hologram. These waveforms drive the rapid charging and discharging of a capacitor in each channel (*In-phase and quadrature*) at every pixel. The net charge over *N* cycles of demodulation frequency is integrated and then digitized to give an in-phase and quadrature value of the temporal oscillations at each pixel. As the digitization of the charge happens after lock-in demodulation, the entire dynamic range of the camera is utilized in recording

the hologram. A comparison of the power mismatch ratios that can be handled by a lock-in camera to that of a traditional camera is presented in Section 3.3.1

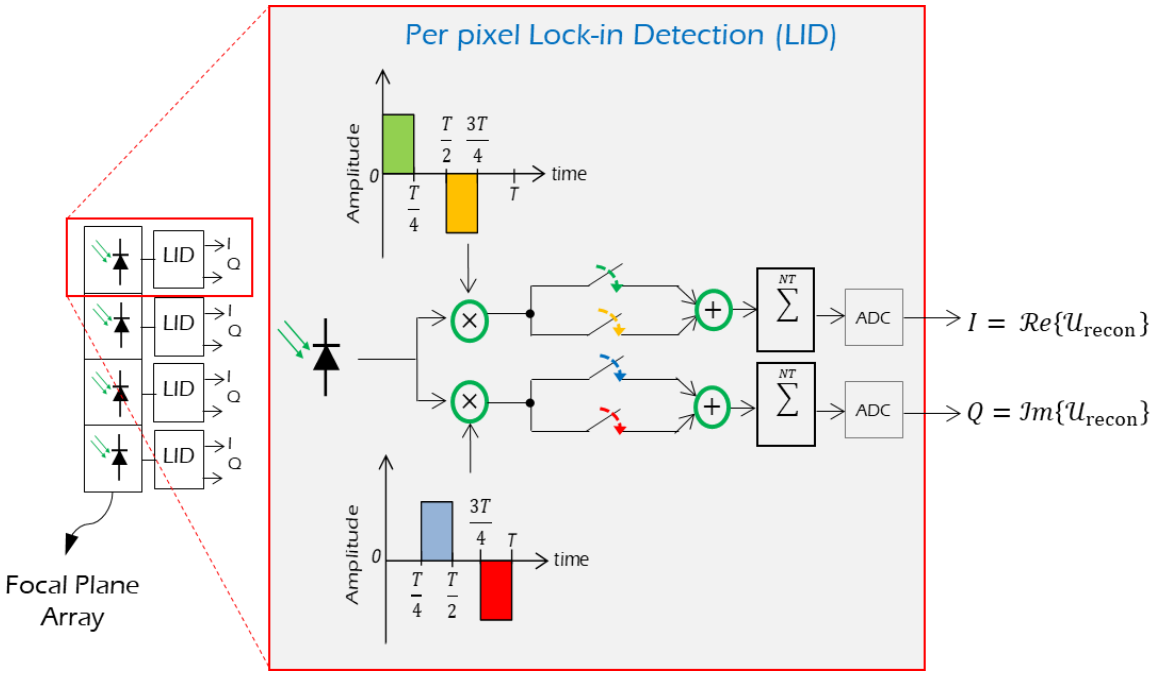

Figure 1-5: Lock-in camera schematic.

1.6 Contributions of this thesis

Use of lock-in focal plane array to circumvent the radiometric losses in indirect imaging:

Experimental validation of the heterodyne interferometry and lock-in based techniques is performed to image objects hidden from view. Analysis of the expected SBR and comparison of the lock-in focal plane array to traditional detectors is presented in the subsequent chapters. Expressions for the SNR are also derived.

Using flutter-shutter camera as an alternative to high speed cameras in performing heterodyne interferometry:

Experimental validation of the heterodyne interferometry using flutter shutter camera is performed to image objects hidden from view. The purpose of this experiment was to understand the impact of a smaller pixel pitch lock-in camera by faking a lock-in demodulation using Flutter shutter camera.

1.7 Organization of the thesis:

The theoretical and experimental details of heterodyne remote digital holography using lock-in camera is presented in Chapter 2. Chapter 3 describes the use of Spatio-temporal holography using flutter-shutter camera to overcome the limitations of the lock-in camera. Chapter 4 introduces the notion of using the lock-in camera and flutter shutter camera in detecting motion of objects around a corner.

Chapter 2

HETERODYNE REMOTE DIGITAL HOLOGRAPHY

The notion of adapting heterodyne interferometry for indirect imaging is explored in this chapter. Theoretical formulation and experimental evidences supporting the heterodyne remote digital holography approach are presented in the following sections.

2.1 Virtual sources and detectors

The indirect imaging approach presented in this thesis closely follows the notion introduced in [15] of converting real-world surfaces such as walls into computational holographic imagers. The approach exploits the fact that most real-world surfaces are rough at the optical wavelengths and hence scatter the incident coherent light into the entire hemisphere. As a result, the hidden object is indirectly illuminated by the coherent light scattered from the wall as illustrated in Figure 2-1.

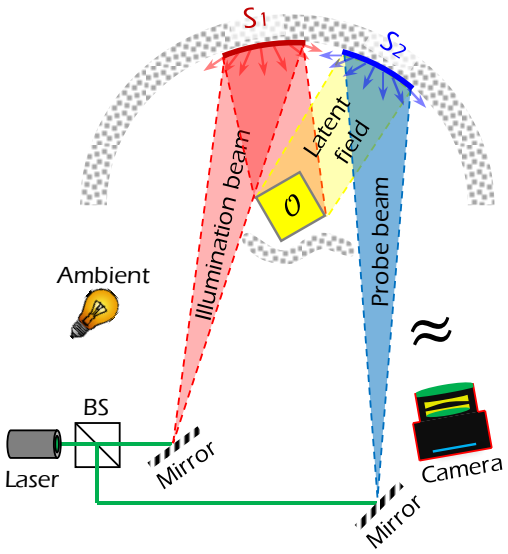

Figure 2-1: Remote Digital Holographic Imager.

Thus, the portion of the wall that indirectly illuminates the hidden object, S_1, can be termed as a virtual source. Similarly, the hidden object scatters the incident light into the hemisphere and is intercepted at a different region of the wall which can then be remotely imaged by a focal plane array. Thus, the portion of the wall that intercepts the scattered return from the hidden object, S_2, can be termed as a virtual detector. The notion of virtualized sources and detectors helps in adapting a class of methods developed for direct line-of-sight imaging to the indirect imaging problem [15]. Although, the roughness of the virtual detector causes additional problems in recovering the object field by scrambling its phase. The problem can be solved by using a coherent reference beam that cancels the phase perturbations introduced by the virtual detector. This forms the basis for the remote digital holography approach presented here. A mathematical model for remote digital holography is presented in the next section.

2.2 Mathematical model

Figure 2-2 illustrates the concept of working of heterodyne remote digital holography. The scattered object field is represented by $\mathcal{U}_{object}(\boldsymbol{r}, t)$, $\boldsymbol{r}$ represents the spatial co-ordinates of points on the virtual detector and t represents the time co-ordinate. Similarly, the reference field is represented by $\mathcal{U}_{reference}(\boldsymbol{r}, t)$. The spatial co-ordinates of the physical detector and the virtual detector are related by the camera magnification as $\boldsymbol{r} = m\boldsymbol{v}_d$. The phase variations associated with the virtual detector surface (or) the complex-valued reflectivity of the virtual detector surface is represented by $\mathcal{R}_{diffuse}(\boldsymbol{r})$.

The instantaneous value of the scattered object field at the virtual detector is expressed as

$$\mathcal{U}_{object}(\boldsymbol{r}, t) = A_{object}(\boldsymbol{r})\mathcal{R}_{diffuse}(\boldsymbol{r}) \exp(-i(\bar{\nu} + \nu_b)t) \qquad (2\text{-}1)$$

$A_{object}(\boldsymbol{r})$ represents the complex amplitude of the scattered object field and $(\bar{\nu} + \nu_b)$ represents the temporal frequency of scattered object field.

Similarly, the instantaneous value of the reference field at the virtual detector can be expressed as

$$\mathcal{U}_{reference}(\boldsymbol{r}, t) = A_{reference}(\boldsymbol{r})\mathcal{R}_{diffuse}(\boldsymbol{r}) \exp(-i\bar{\nu}t) \tag{2-2}$$

$A_{reference}(\boldsymbol{r})$ represents the complex amplitude of the reference field and $\bar{\nu}$ represents the temporal frequency of reference field.

It can be observed from Equation (2-1) and Equation (2-2) that the scattered object field and the reference field are oscillating at different temporal frequencies. The instantaneous field at the virtual detector is a superposition of the reference field and the scattered object field and is given by,

$$\mathcal{U}_{VD}(\boldsymbol{r}, t) = \mathcal{U}_{reference}(\boldsymbol{r}, t) + \mathcal{U}_{object}(\boldsymbol{r}, t) \tag{2-3}$$

This field at the virtual detector relayed remotely to a physical detector by imaging optics with a space invariant amplitude point spread function represented by $h_{cam}(x)$.

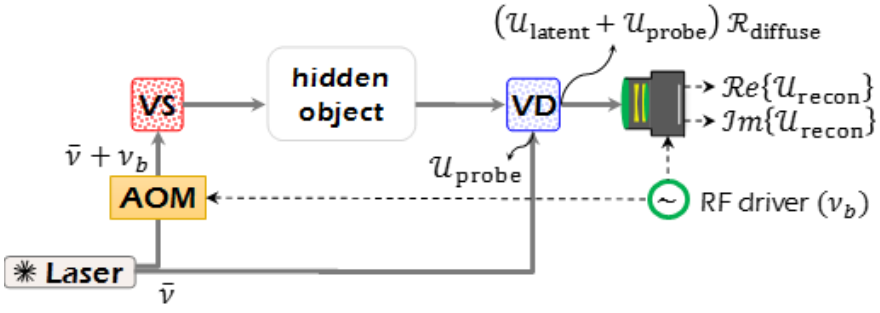

Figure 2-2: Heterodyne Remote Digital Holography Schematic.

Thus, the field at the physical detector expressed as

$$\mathcal{U}_{cam}(\boldsymbol{x},t)=\int_{\mathcal{A}} d\boldsymbol{r}\ \left\{\mathcal{R}_{diffuse}(r)\begin{pmatrix}\mathcal{U}_{reference}(r,t)\ +\\ \mathcal{U}_{object}(r,t)\end{pmatrix}\right\}h_{cam}(x-r) \tag{2-4}$$

The irradiance at the detected by the camera can be expressed as,

$$i_{cam}(\boldsymbol{x},t)=\left|\int_{\mathcal{A}} d\boldsymbol{r}\ \left\{\mathcal{R}_{diffuse}(\boldsymbol{r})\begin{pmatrix}\mathcal{U}_{reference}(\boldsymbol{r},t)\ +\\ \mathcal{U}_{object}(\boldsymbol{r},t)\end{pmatrix}\right\}h_{\text{cam}}(\boldsymbol{x}-\boldsymbol{r})\right|^2 \tag{2-5}$$

Substituting Equation (2-1) and Equation (2-2) in Equation (2-5), the expression for the instantaneous irradiance detected by the camera is given by,

$$i_{cam}(\boldsymbol{x},t)$$
$$=\begin{Bmatrix}\left|A_{object}(\boldsymbol{x})\mathcal{R}_{diffuse}(\boldsymbol{x})\otimes h_{cam}(\boldsymbol{x})\right|^2+\left|A_{reference}(\boldsymbol{x})\mathcal{R}_{\text{diffuse}}(\boldsymbol{x})\otimes h_{cam}(\boldsymbol{x})\right|^2\\ +\exp(i\upsilon_b t)\times\left(A_{object}(\boldsymbol{x})\mathcal{R}_{diffuse}(\boldsymbol{x})\otimes h_{cam}(\boldsymbol{x})\right)\times\text{conj}\left(A_{reference}(\boldsymbol{x})\mathcal{R}_{diffuse}(\boldsymbol{x})\otimes h_{cam}(\boldsymbol{x})\right)\\ +\exp(-i\upsilon_b t)\times\left(A_{reference}(\boldsymbol{x})\mathcal{R}_{diffuse}(\boldsymbol{x})\otimes h_{cam}(\boldsymbol{x})\right)\times\text{conj}\left(A_{object}(\boldsymbol{x})\mathcal{R}_{diffuse}(\boldsymbol{x})\otimes h_{cam}(\boldsymbol{x})\right)\end{Bmatrix} \tag{2-6}$$

The first two terms in Equation (2-6) represent the zeroth order contribtion. The third and fourth terms represent the hologram its twin contribution. It can be observed that the hologram term oscillates at a distinct temporal frequency, υ_b. A synchronous demodulation strategy introduced in Section 1.4 exploiting the orthogonality of complex sinusoids is adopted to isolate the hologram term from the other terms.

2.3 Frequency diversity between the interfering beams

This section briefly describes some of the important methods used to achieve the frequency diversity between the interfering beams for heterodyne holography method introduced before. A detailed description of the methods to introduce frequency diversity can be found in [34]:

- Zeeman lasers: Zeeman lasers are dual frequency lasers which emit two frequency shifted laser beams simultaneously at their output. They rely on the "Zeeman effect" to split a single laser mode into two beams with shifted frequencies. These two split beams have orthogonal circular polarization states and hence can be separated easily. A single Zeeman laser can directly be used to do heterodyne interferometry. The important disadvantage with using these lasers is the fact that they operate only at certain wavelengths and the frequency difference of the order of 1.8 – 5 MHz which is very high for demodulating using the commercial of-the-shelf lock-in camera.
- Moving mirrors/gratings: Light reflecting off the mirrors moving at a constant velocity introduce a frequency shift proportional to the velocity of motion. Moving diffraction gratings also produce the same doppler frequency shifts in the diffracted orders and produce the required frequency diversity. But, presence of moving mechanical elements can result in errors and spurious vibrations. Also, the frequency shifts are limited to low frequencies.
- Acousto optic modulators: Acousto optic modulators rely on the periodic refractive index variations created by an acoustic wave travelling through a Bragg crystal to produce frequency shifts. When a laser beam interacts with this periodic change in refractive index, it splits into different orders. Each order undergoes a different frequency shift due to the doppler shifts experienced while travelling through the medium. These can be used over a wide variety of wavelengths and do not have any mechanical moving parts.

In our experiments, we have used a pair of AOMs to generate the frequency shifts of interest in the KHz range. The laser beam passing through the first AOM is upshifted in frequency and get downshifted while passing through the second AOM. The net frequency shift can be adjusted to

be within the KHz range for the lock-in camera demodulation. The schematic of the AOM setup is shown in Figure 2-3.

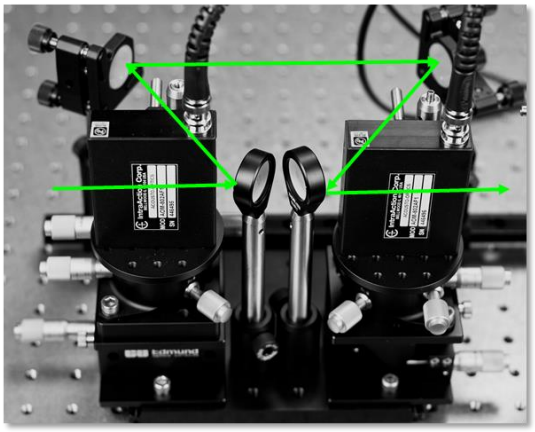

- AOM Intraaction 802-AF1
- Dual channel frequency synthesizer
- Clear aperture ~ 2 mm
- 60 MHz – 100 MHz
- f = 80 MHz
- λ = 532 nm

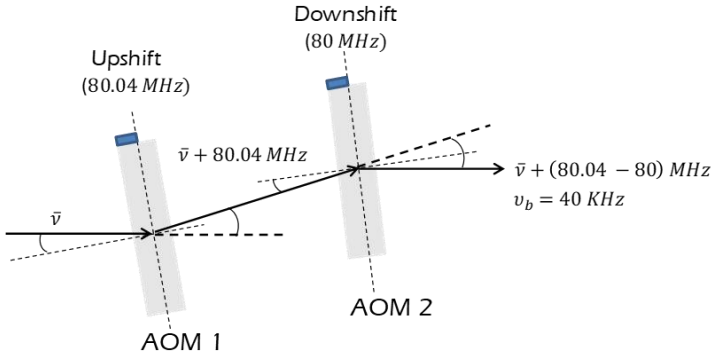

The drive frequencies for the two AOMs are phase locked

Figure 2-3: Schematic of the cascaded AOMs.

The first experimental validation of the proposed approach is done in transmission geometry to recover the image of an object hidden behind a ground glass diffuser. The experimental details and the results of the experiment are presented in the next section.

2.4 Indirect Imaging in transmission mode using the lock-in camera

The hologram of a transmissive resolution target hidden behind a ground glass diffuser is extracted based on an adaptation of Mach-Zehnder interferometer [33] as illustrated in Figure 2-4. A 532nm linearly-polarized collimated laser source (*Vortran Stardus 532 - 40, beam diameter 0.8 mm*) is split into a reference arm and the object arm. A cascade of AOMs (*Intraaction AOM-802AF1*) is used to upshift the temporal frequency of the illumination beam by 40 *KHz*, relative to the temporal frequency of the reference beam. The emerging beam from the AOM is expanded using a 5X Beam expander. An USAF resolution target (*Newport RES-1*) inserted in the illumination path serves as the hidden object. Light from the two interferometer arms is combined using a non-polarizing beam splitter before being directed towards a diffuser (*Thorlabs DG100X100 -220*) acts as a virtual detector. The lock-in camera (*Heliotis Helicam C3*) demodulates the light distribution at the

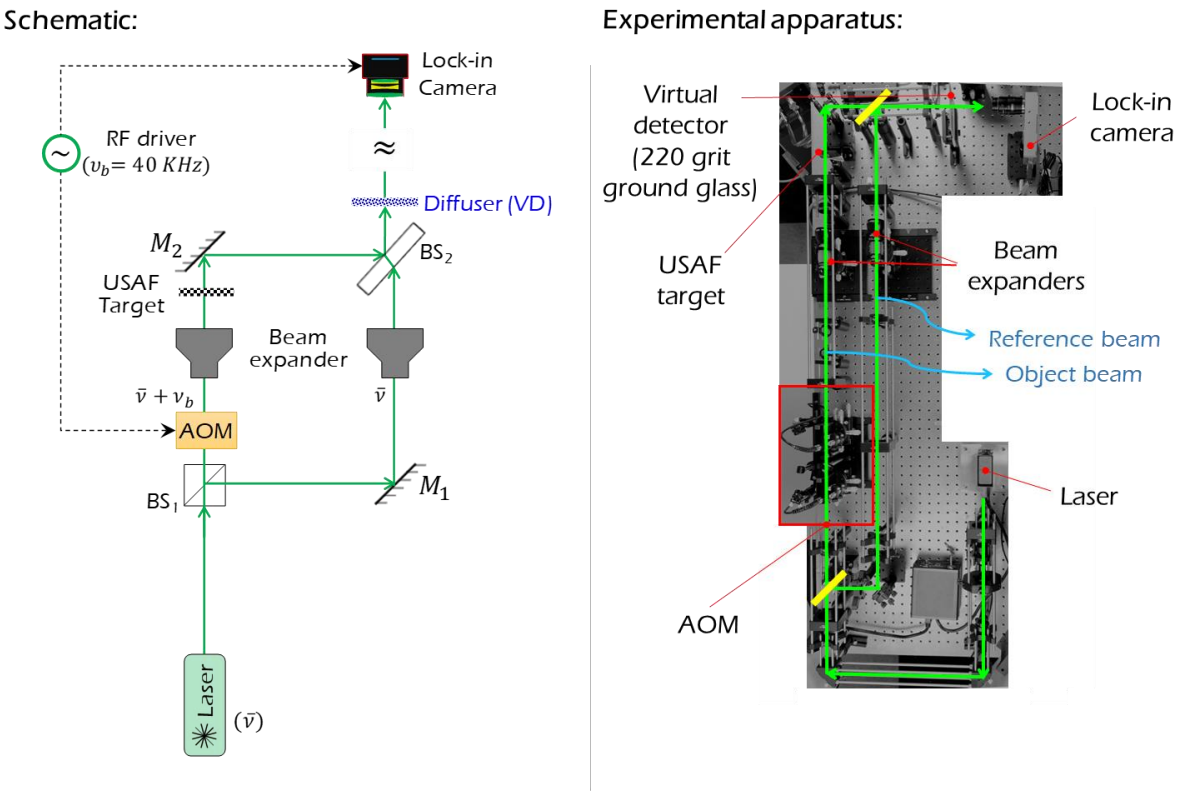

Figure 2-4: Transmission mode heterodyne RDH schematic and setup.

diffuse to latent hologram of the target hidden from view. The real and imaginary components of the acquired latent hologram are shown in the image insets of Figure 2-5. Using the proposed approach, element 5 in group 1 of the USAF target could be fully resolved following back-propagation from the diffuser plane to the hidden target plane.

Thus, using this experiment, it is established that the heterodyne remote digital holography approach can be used to image objects hidden behind a diffuser. Next section describes the extension of this experiment to reflection mode geometry.

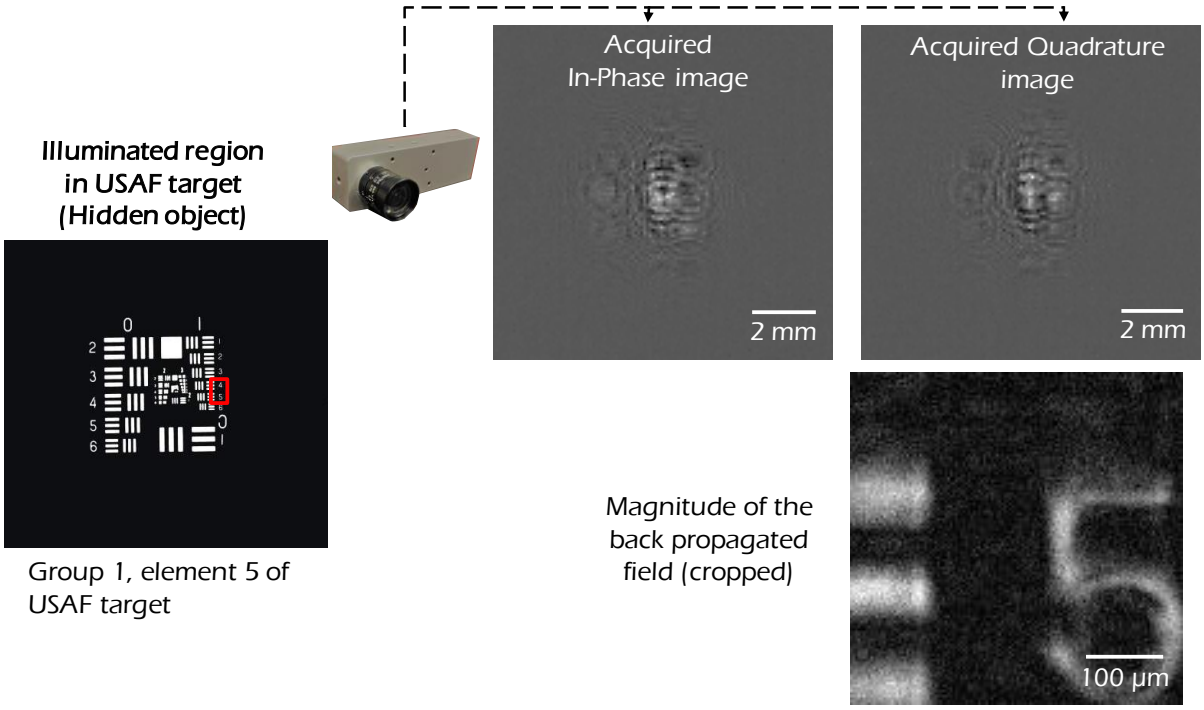

Figure 2-5: Transmission mode heterodyne RDH results.

2.5 Indirect Imaging in reflection mode using the lock-in camera

Figure 2-6 illustrates the schematic of the setup used to extract the hologram of a resolution target occluded from view in a reflection mode geometry. The output beam from a collimated laser source

(*Vortran Stradus 532 nm, 40 mW, Ø1 mm*) is split into the reference and the object beams using a non-polarizing 50:50 cube beam splitter. A frequency shift of 70 *KHz* is introduced in the object beam by passing it through a cascade of two Acousto-optic modulators (*Intraaction AOM-802AF1*). Both the object beam and the reference beam are expanded using 5X beam expanders. The object beam is directed towards the rough mirror. The rough mirror acts as a virtual source by diffusely illuminating the hidden object. The hidden object in this experiment is a reflective USAF target (*Edmund Optics #38-257*) placed between the virtual source and virtual detector. The hidden object was placed about 0.8 meters behind the virtual detector.

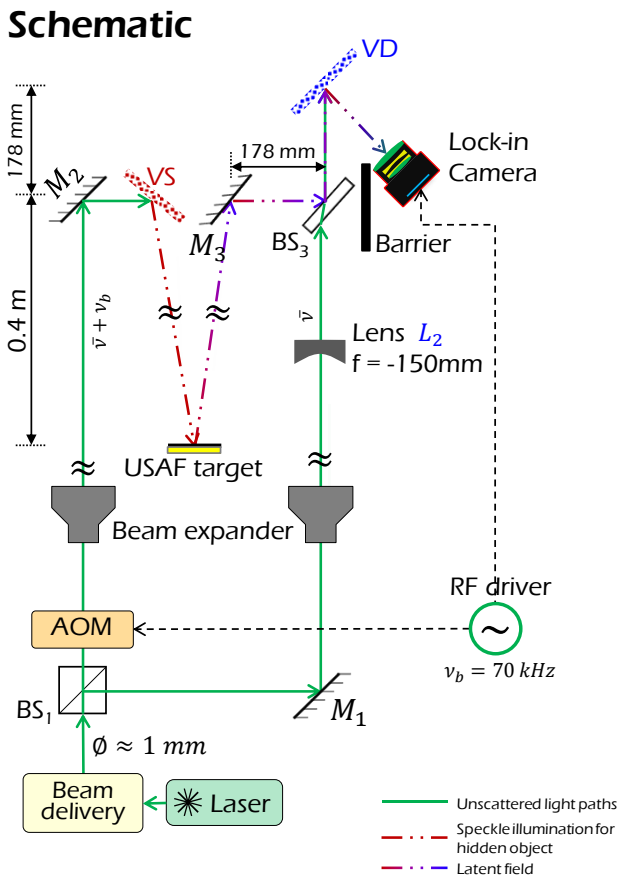

Figure 2-6: Reflection mode heterodyne RDH schematic.

The expanded beam in the reference arm is directed through a 150-mm bi-concave diverging lens to creates a virtual focus at the axial location of the object plane. The reference field and the object field are recombined using a plate beam splitter and are directed towards a Silver foil, acting as a virtual detector. The choice of silver foil as virtual detector was made to improve the light throughput at the lock-in camera. Diffraction limited imaging optics (*Thorlabs MVL 50TM23*) is used to relay the fringe pattern observed at the virtual detector to the lock-in camera (*Heliotis Helicam C3*). The magnification of the imager was about 0.4. The lock-in camera outputs an in-phase and quadrature image by demodulating the irradiance over 82 cycles at 70 *KHz* demodulation frequency. 100 successive frames of the latent hologram were averaged to improve the SNR of reconstruction. The image of the object is reconstructed by computing the magnitude of the Fourier transform of the averaged latent hologram. As illustrated in Figure 2-7, reconstructions with a resolution of the order of 500 µm at 0.8 meters standoff are achieved using

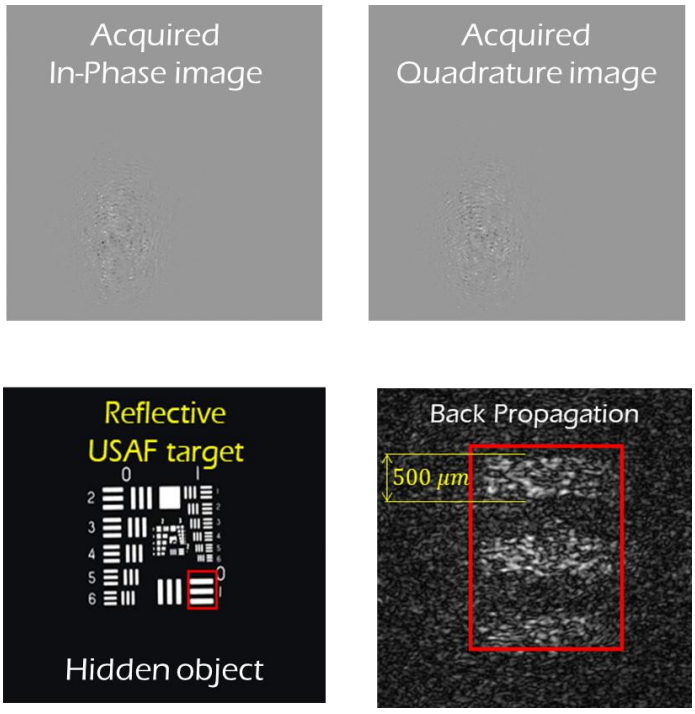

Figure 2-7: Reflection mode heterodyne RDH results.

this approach. The results of the experiment reaffirm the notion that the latent object information can be reconstructed even under very low signal to background ratios and with excellent temporal resolution using heterodyne RDH. The following section discusses the performance metrics of the heterodyne RDH setup such as the field of view (FOV), resolution and presents an analysis of SNR.

2.6 Performance limitations of the heterodyne remote digital holography

Remote digital holography is predicated on the fact that the random phase perturbations introduced by the virtual detector surface to the object beam are compensated for by the reference beam. The phase of the hologram is the phase of the object beam with respect to a known reference. Hence, if the reference beam undergoes the same phase perturbation as the object beam, the effect of scattering at VD can be circumvented to obtain the holographic description of the hidden object. This assumption is valid only to a small range of angular separations between the reference beam and the object beam. As the angular separation increases, the path length variations introduced by the VD to the reference beam and the object beam are no longer identical resulting in a scrambling of phase of the hologram. The angular separations over which the path length variations introduced are largely identical is termed as isoplanatic angle of the virtual detector surface [40]

Assuming both the reference and the object beams are within the isoplanatic angle of the virtual detector surface, the FOV and the resolution of the reconstruction for various angular offsets between the object and the reference beam are discussed in the following section for the lock-in camera.

2.6.1 FOV and resolution of reconstruction using Lock-in camera

Figure 2-8 illustrates the Heterodyne RDH scenario used to derive the FOV and the resolution. The spherical waves emerging the extreme object point (X_{max}, Y_{max}, Z_r) and the reference point

(X_r, Y_r, Z_r) interfere to produce a fringe on VD, with spatial frequency $\left(\frac{X_{\max}-X_r}{\lambda Z_r}, \frac{Y_{\max}-Y_r}{\lambda Z_r}\right)\frac{\text{cyc}}{\text{mm}}$. This determines the upper bound on the inter-sample spacing $\sqrt{A_{pix}}$ (*assuming square pixels of area* A_{pix}) required to record a latent hologram of the hidden object without aliasing. Even higher spatial frequencies will not even pass through the imager and hence are blurred and not recorded. It can be seen that $\sqrt{A_{pix}} \leq \min\left(\frac{\lambda Z_r}{2(X_{\max}-X_r)}, \frac{\lambda Z_r}{2(Y_{\max}-Y_r)}\right)$.

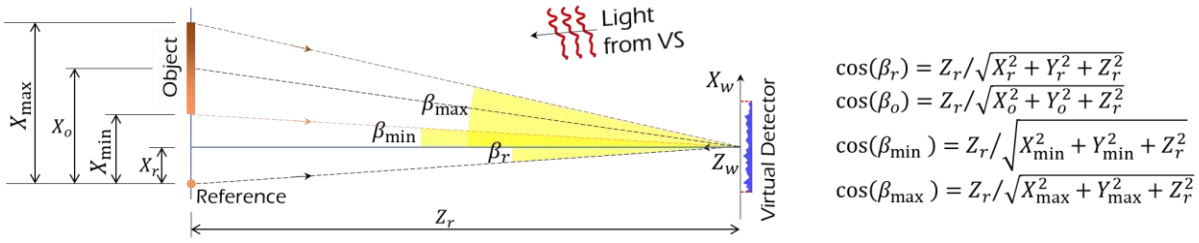

Figure 2-8: Canonical scene for evaluating the performance limits
(Image reproduced with permission from Reference 21).

The FOV of the RDH system is limited by the isoplanatic angle of VD and the lateral separation of the reference point source with respect to the object. In the case of RDH using the lock-in camera, the FOV is largely limited by the large inter-sample spacing of the lock-in camera and the isoplanatic angle of the VD plays a small role. As the reference point source gets closer to the object, the FOV attains a maximum.

As seen from the discussion above, where it is shown that the sampling frequency on the VD determines the FOV of the imager, the same principle when applied in reverse would determine the resolution of the RDH imager. This is due to the fact that in Fourier transform holography, the

hologram plane and the reconstruction plane are Fourier transforms of each other. Hence, the spatial resolution of reconstruction is determined by the extent of the hologram. The area of the captured hologram would determine the finest spatial frequency that can be attained in the reconstructed image. This directly gives the resolution of the heterodyne RDH setup. Supposing the extent of the hologram is $M\sqrt{A_{pix}} \times M\sqrt{A_{pix}}$, the resolution on the reconstruction is given by $\frac{\lambda Z_r}{M\sqrt{A_{pix}}}\mu m$ [1]. It should be noted although that the resolution is the maximum resolution attainable in the absence of speckle noise. When in presence of speckle, the resolution is fundamentally limited by the average speckle grain size on the reconstruction.

Wavelength $= 0.532\mu m$

Parameter	$Z_r = 1m$	$Z_r = 1m$
Inclination of reference β_r	0°	0.1°
Magnification, M	0.51	0.51
Size of hologram $S\ mm \times S\ mm$	24.6×24.6	24.6×24.6
Minimum inter sample(ISS) spacing at VD $\sqrt{A_{pixel}}$	$76.2\mu m$	$76.2\mu m$
$\beta_{\min}$, $\beta_{\max}$	$0^\circ, -0.2^\circ$	$0^\circ, -0.1^\circ$
Maximum size of hidden object $X_{\max} - X_{\min}$	$3.4\ mm$	$1.74\ mm$
Minimum achievable resolution on target	$21.6\ \mu m$	$21.6\ \mu m$

Figure 2-9 FOV and resolution of lock-in camera

In the Heterodyne RDH experiments in reflection mode, 500 µm bars occupied ~37 pixels in area resulting in an effective resolution of ~14 µm (*A magnification of 0.5 is assumed in the analysis which is closer to 0.4 magnification used in the experiments*). As can be seen from the discussion above, the maximum angular separation tolerable with the lock-in camera is of the order of 0.1°. This significantly limits the FOV and the type of scenes for which this approach can be used. Another performance criteria for the RDH system in terms of the SNR analysis is presented in the next section.

2.6.2 Noise in heterodyne RDH

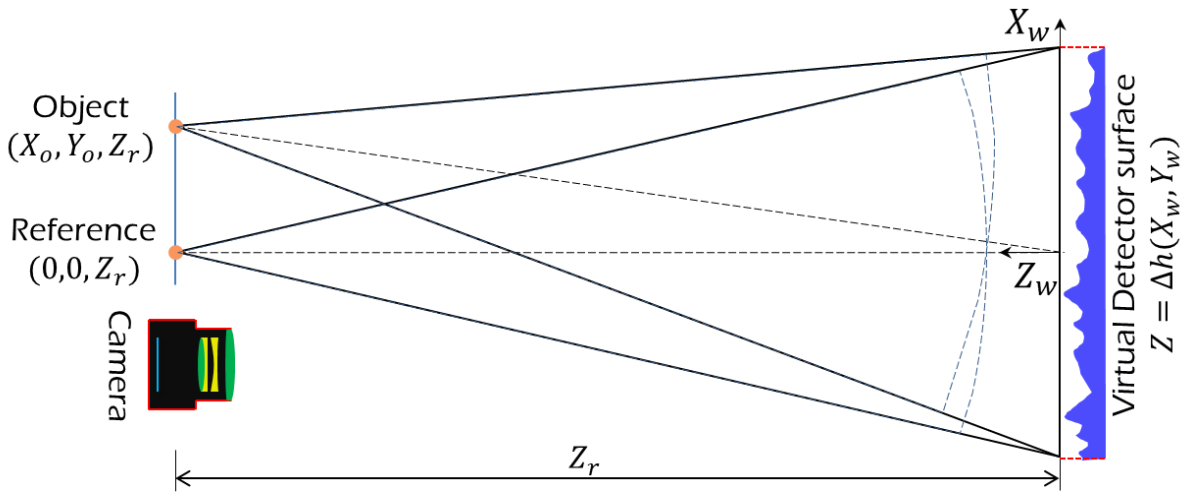

Figure 2-10: Heterodyne RDH schematic for noise analysis.

The noise analysis presented in this section closely follows the approach of reference [28]. In the case of RDH, due to the roughness of wall and imaging optics, the two interfering fields on the camera are speckle fields. Let, $\mathcal{U}_{reference}(X_W, Y_W)$ and $\mathcal{U}_{object}(X_W, Y_W)$ be the two fields illuminating the virtual detector surface.

The reference field from the point source located at $(0,0,Z_r)$ can be represented as,

$$\mathcal{U}_{reference}(X_W, Y_W)$$

$$= \left(\frac{exp(ikZ_r)}{i\lambda Z_r} exp\left(\frac{ik}{2Z_r}\left[{X_w}^2 + {Y_w}^2\right]\right)\right) \times (exp(ik[1 + cos(\beta_r)]\Delta h(X_w, Y_w))) \quad (2\text{-}7)$$

Where, $[\sin(\beta_r)\cos(\alpha_r), \sin(\beta_r)\sin(\alpha_r), \cos(\beta_r)]$ are the direction cosines of the reference field and $\cos(\beta_r)\,\Delta h(X_w, Y_w)$ is the path length experience by the beam from the reference surface Z_w to the virtual detector. Equation (2-7) can be seperated in terms of the reference amplitude component, $\mathcal{U}_{sph}$ and the VD component as $\mathcal{U}_{VD}$

$$\mathcal{U}_{reference}(X_W, Y_W) = \mathcal{U}_{sph}(X_W, Y_W) \times \mathcal{U}_{VD}(X_W, Y_W, \beta_r) \quad (2\text{-}8)$$

Similarly, the object field from the point source located at (X_o, Y_o, Z_r) can be represented as,

$$\mathcal{U}_{object}(X_W, Y_W)$$

$$= \sqrt{\kappa}\left(\frac{exp(ikZ_r)}{i\lambda Z_r} exp\left(\frac{ik}{2Z_r}\begin{bmatrix}(X_w - X_o)^2 + \\ (Y_w - Y_o)^2\end{bmatrix}\right)\right) \quad (2\text{-}9)$$

$$\times (exp(ik[1 + cos(\beta_o)]\Delta h(X_w, Y_w)))$$

Here, κ is the power mismatch in intensity of the two fields. Equation (2-9) can be seperated in terms of the reference amplitude component, additional phase component due to tilt and the VD component as,

$$\mathcal{U}_{object}(X_W, Y_W)$$

$$= \sqrt{\kappa}\mathcal{U}_{sph}(X_W, Y_W) \times exp\left(\frac{ik}{2Z_r}\left[{X_o}^2 + {Y_o}^2\right]\right) \times exp\left(\frac{-ik}{Z_r}[X_o X_w + Y_o Y_w]\right) \quad (2\text{-}10)$$

$$\times\ \mathcal{U}_{VD}(X_W, Y_W, \beta_0)$$

These fields are imaged on to the camera using a lens with an amplitude PSF represented by $h_{cam}(X, Y;\ X_W, Y_W)$ [1].

The field due to the reference point source on the camera can be represented as,

$$\mathcal{U}^{cam}_{reference}(X,Y) = \iint_{-\infty}^{\infty} \mathcal{U}_{reference}(X_W, Y_W)\, h_{cam}(X - X_W, Y - Y_W) dX_w dY_w \tag{2-11}$$

$$= \iint_{-\infty}^{\infty} \mathcal{U}_{sph}(X_W, Y_W) \times \mathcal{U}_{VD}(X_W, Y_W, \beta_r)\, h_{cam}(X - X_W, Y - Y_W) dX_w dY_w \tag{2-12}$$

Similarly, the object field on the camera can be represented as,

$$\mathcal{U}^{cam}_{object}(X,Y)$$

$$= \sqrt{\kappa} \iint_{-\infty}^{\infty} \left\{ \begin{matrix} exp\left(\frac{ik}{2Z_r}\left[{X_o}^2 + {Y_o}^2\right]\right) \times exp\left(\frac{-ik}{Z_r}\left[X_o X_w + Y_o Y_w\right]\right) \mathcal{U}_{sph}(X_W, Y_W) \\ \times \mathcal{U}_{VD}(X_W, Y_W, \beta_0) \times\ h_{cam}(X - X_W, Y - Y_W) \end{matrix} \right\} dX_w dY_w \tag{2-13}$$

$$= \sqrt{\kappa}\, exp\left(\frac{ik}{2Z_r}\left[{X_o}^2 + {Y_o}^2\right]\right) \iint_{-\infty}^{\infty} \left\{ \begin{matrix} \mathcal{U}_{sph}(X_W, Y_W) \times \mathcal{U}_{VD}(X_W, Y_W, \beta_0) \\ \times\ h_{cam}(X - X_W, Y - Y_W) \end{matrix} \right\} dX_w dY_w \tag{2-14}$$

The interference of these fields on the camera can be represented by,

$$I(X,Y) = \left| \mathcal{U}^{cam}_{reference}(X,Y) + \mathcal{U}^{cam}_{object}(X,Y) \right|^2 \tag{2-15}$$

As the fields are stochastic in nature, to measure the strength of the interference term, an ensemble average of intensity measurements (*for example: if the wall is moving or by scanning the beams*) is performed to obtain,

$$\langle I(X,Y) \rangle = \left\{ \begin{matrix} \langle I^{cam}_{reference}(X,Y) \rangle + \langle I^{cam}_{object}(X,Y) \rangle \\ \langle \mathcal{U}^{cam}_{reference}(X,Y) \times conj\left(\mathcal{U}^{cam}_{object}(X,Y)\right) \rangle \\ \langle \mathcal{U}^{cam}_{object}(X,Y) \times conj\left(\mathcal{U}^{cam}_{reference}(X,Y)\right) \rangle \end{matrix} \right\} \tag{2-16}$$

The hologram term of interest can be obtained as,

$$\langle \mathcal{U}^{cam}_{reference}(X,Y) \times conj\left(\mathcal{U}^{cam}_{object}(X,Y)\right)\rangle$$

$$= \sqrt{\kappa} \int_{-\infty}^{\infty}\int_{-\infty}^{\infty} \left\{ \begin{matrix} \mathcal{U}_{sph}(X_W,Y_W)\mathcal{U}^{*}_{sph}(\acute{X_W},\acute{Y_W})\langle \mathcal{U}_{VD}(X_W,Y_W,\beta_r)\mathcal{U}^{*}_{VD}(\acute{X_W},\acute{Y_W},\beta_0)\rangle \\ \times h_{cam}(X - X_W, Y - Y_W) \times h^{*}_{cam}(X - \acute{X_W}, Y - \acute{Y_W}) \\ \times exp\left(\frac{-ik}{Z_r}[X_o X_w + Y_o Y_w]\right) \end{matrix} \right\} \begin{matrix} dX_w dY_w \\ \times d\acute{X}_W d\acute{Y}_W \end{matrix} \quad (2\text{-}17)$$

In obtaining the above expression, the constant phase term $exp\left(\frac{ik}{2Z_r}\left[{X_o}^2 + {Y_o}^2\right]\right)$ is neglected. The complex valued reflectivity for the two beams can be assumed to be the same as long they are within the isoplanatic angle of the virtual detector surface. Thus,

$$\mathcal{U}_{VD}(X_W,Y_W,\beta_r) = \mathcal{U}_{VD}(X_W,Y_W,\beta_o) \quad (2\text{-}18)$$

Now, the cross correlation of the complex valued reflectivity's can be approximated to be a dirac delta function with a finite correlation value as the VD surface is rough at optical scales resulting in,

$$\langle \mathcal{U}_{VD}(X_W,Y_W,\beta_r)\mathcal{U}^{*}_{VD}(\acute{X_W},\acute{Y_W},\beta_0)\rangle = \delta(X_W - \acute{X_W}) \quad (2\text{-}19)$$

Equation (2-17) can be simplified using Equation (2-19) to be

$$\langle \mathcal{U}^{cam}_{reference}(X,Y) \times conj\left(\mathcal{U}^{cam}_{object}(X,Y)\right)\rangle$$

$$= \sqrt{\kappa} \int_{-\infty}^{\infty} \left\{ \begin{matrix} \left|\mathcal{U}_{sph}(X_W,Y_W)\right|^2 \\ \times exp\left(\frac{-ik}{Z_r}[X_o X_w + Y_o Y_w]\right)|h_{cam}(X - X_W, X - Y_W)|^2 \end{matrix} \right\} dX_w dY_w \quad (2\text{-}20)$$

$\left|\mathcal{U}_{sph}(X_W,Y_W)\right|^2$ is the intensity of the spherical wave is a constant. Thus, the resulting equation is a convolution of the phase difference between the two fields with the intensity PSF of the imager. In the frequency domain it is the product of the OTF of the imaging system and the Fourier transform of the spatial frequency of the phase difference [1]. So, the result would be the phase

multiplied by a complex factor as determined by the OTF of the imaging system. For the purposes of this derivation, the phase carrier is assumed to be within the cutoff frequency of the OTF and hence the resulting hologram term can be expressed as,

$$\begin{aligned}\langle I^{cam}_{hologram}(X,Y)\rangle &\propto \sqrt{\kappa}\left|\mathcal{U}_{sph}(X,Y)\right|^2 \, exp\left(\frac{-ik}{Z_r}[X_o X + Y_o Y]\right) \\ &\propto \sqrt{\kappa}\left|\mathcal{U}_{sph}(X,Y)\right|^2 \, exp(-i\,\phi(X,Y))\end{aligned} \tag{2-21}$$

In heterodyne Interferometry, this hologram term is oscillating at a beat frequency ν_b. Hence, the hologram term becomes,

$$\begin{aligned}\langle I^{cam}_{hologram}(X,Y)\rangle &= \sqrt{\kappa}\left|\mathcal{U}_{sph}(X,Y)\right|^2 exp(i\,\{2\pi\nu_b t - \phi(X,Y)\}) \\ &= \sqrt{\kappa}\,\langle\left|I_{reference}(X,Y)\right|\rangle\, exp(i\,\{2\pi\nu_b t - \phi(X,Y)\})\end{aligned} \tag{2-22}$$

Where,

$$\langle\left|I_{reference}(X,Y)\right|\rangle = \langle \mathcal{U}^{cam}_{reference}(X,Y) \times conj\left(\mathcal{U}^{cam}_{object}(X,Y)\right)\rangle \tag{2-23}$$

Expanding Equation(2-23) using Equation (2-12) and following the same assumptions as in Equation(2-19), we get,

$$\langle\left|I_{reference}(X,Y)\right|\rangle = \iint_{-\infty}^{\infty}\left|\mathcal{U}_{sph}(X_W,Y_W)\right|^2 |h_{cam}(X - X_W, X - Y_W)|^2 dX_w dY_w \tag{2-24}$$

Or,

$$\langle\left|I_{reference}(X,Y)\right|\rangle = \left|\mathcal{U}_{sph}(X_W,Y_W)\right|^2 \tag{2-25}$$

$\langle\left|I_{reference}(X,Y)\right|\rangle$ and $\langle\left|I_{object}(X,Y)\right|\rangle$ represent the mean intensity of the reference and object speckle fields interfering in the detector, which from Equation(2-25), can be seen to be equivalent to an incoherent image of the illumination [22].

If the complex valued reflectivity of the wall is not the same for both the beams, then the peak value of the correlation $\langle \mathcal{U}_{VD}(X_W, Y_W, \beta_r)\mathcal{U}^*_{VD}(\acute{X_W}, \acute{Y_W}, \beta_0)\rangle$ in Equation (2-19) would drop resulting in a drop in signal amplitude.

Upon demodulation of the hologram term over N cycles using a sine and cosine waveforms, the in-phase and quadrature terms become (*see Appendix*),

$$I_{in-phase}(X,Y) = \frac{2N\sqrt{\kappa}}{\pi\nu_b}\,\langle|I_{reference}(X,Y)|\rangle\, cos(\phi(X,Y)) \tag{2-26}$$

$$I_{quadrature}(X,Y) = \frac{2N\sqrt{\kappa}}{\pi\nu_b}\,\langle|I_{reference}(X,Y)|\rangle\, sin(\phi(X,Y)) \tag{2-27}$$

As the signal amplitude is measured using an ensemble of measurements even the reference intensity is uniform and not speckle. Hence, the dominant source of noise is from the shot noise. Assuming the reference beam is significantly stronger than the object beam, the signal is limited by the shot noise from the reference beam as all the other sources of noise are small. The shot noise is proportional to the square-root of the signal strength within the exposure time. As the signal power is measured over an ensemble of measurements, even the reference power can be measured in a similar way, to get,

$$I_{noise}(X,Y) \approx \frac{1}{4\nu_b}\sqrt{\langle|I_{reference}(X,Y)|\rangle} \tag{2-28}$$

Computing the ratio of the signal to noise amplitudes, and converting into number of photoelectrons, we get,

$$SNR = \frac{N\sqrt{\kappa}}{2\pi}\sqrt{\langle|I_{reference}(X,Y)|\rangle\left(\frac{A_{pixel}\eta\tau}{h\upsilon}\right)} \tag{2-29}$$

Where, η represents the quantum efficiency of the detector, τ represents the exposure time per quarter demodulation cycle over which the shot noise is estimated and $h\upsilon$ represents the energy of each photon.

But, as mentioned earlier in the derivation, the reference and object beam intensities are related by a power mismatch factor κ,

$$\langle |I_{object}(X,Y)| \rangle = \kappa \langle |I_{reference}(X,Y)| \rangle \tag{2-30}$$

Hence, Equation (2-29) can be rewritten as,

$$SNR = \frac{N}{2\pi} \sqrt{\langle |I_{object}(X,Y)| \rangle \left(\frac{A_{pixel}\eta\tau}{h\upsilon}\right)} \tag{2-31}$$

It can be seen that the SNR is proportional to the number of demodulation cycles as with traditional heterodyne interferometry [24]. It is also worth mentioning that from Section 2.6.1 for larger FOV we require smaller pixel area, whereas, from Equation (2-31), it can be seen that for higher SNR, we require larger pixel area. This trade-off has to be kept in mind when choosing the correct pixel pitch for the RDH imager.

2.6.3 Lock-in camera limitations

Apart from the discussed limitations, there is a maximum exposure time limitation in the commercially available lock-in camera. According to the manufacturer, due to the internal circuitry mechanisms, the lock-in camera readings are only reliable up to ~100 demodulation cycles. This limits the maximum exposure time for which the lock-in camera can be exposed.

2.7 Summary

The theoretical model and the supporting experimental results presented in this chapter confirm the notion that indirect imaging can be performed by converting scattering surfaces into computational holographic imagers. Heterodyne remote digital holography using lock-in camera presents a credible approach towards recovering the hologram of the hidden object even under weak signal to background conditions. The limitations of the currently available lock-in camera are discussed and a workaround for the large pixel pitch problem is proposed in the next chapter.

Chapter 3

SPATIO-TEMPORAL HOLOGRAPHY USING FLUTTER SHUTTER CAMERA

As described in the Chapter 2, one of the most important limitations of the lock-in camera is its large pixel pitch which poses challenges in recovering the spatial details of the hologram at high resolution. The purpose of the line of approach taken in this chapter is to analyze the impact a smaller pixel pitch lock-in camera should one exist. To simulate the functioning of a lock-in camera with a smaller pixel pitch, a flutter shutter camera is used to perform heterodyne remote digital holography.

Flutter shutter cameras are originally developed for motion deblurring applications [36]. By coding the exposure time using a pseudo random code (m-sequence etc.), the higher temporal frequency information detail is preserved in the captured image. The knowledge of the code is then utilized to deblur the captured image and overcome the motion blur. The lock-in camera can also be considered as a coded exposure camera except that the demodulation code is a specific binary periodic sequence. The flutter shutter camera is coded to demodulate the heterodyne signal using a square wave demodulation.

3.1 Mathematical Model

The workflow of spatio-temporal holography using flutter shutter camera is illustrated in Figure 3-2. The scattered object field is represented by $\mathcal{U}_{object}(\boldsymbol{r}, t)$, $\boldsymbol{r}$ represents the spatial co-ordinates of points on the virtual detector and t represents the time co-ordinate. Similarly, the reference field is represented by $\mathcal{U}_{reference}(\boldsymbol{r}, t)$. The spatial co-ordinates of the physical detector and the virtual detector are related by the camera magnification as $\boldsymbol{r} = m\boldsymbol{v}_d$. The phase variations

associated with the virtual detector surface (or) the complex-valued reflectivity of the virtual detector surface is represented by $\mathcal{R}_{diffuse}(\boldsymbol{r})$.

The instantaneous value of the scattered object field at the virtual detector is expressed as

$$\mathcal{U}_{object}(\boldsymbol{r},t) = A_{object}(\boldsymbol{r})\mathcal{R}_{diffuse}(\boldsymbol{r}) \exp\left(-i\left((\bar{\nu}+\nu_b)t - \phi_{obj}(\boldsymbol{r})\right)\right) \quad (3\text{-}1)$$

$A_{object}(\boldsymbol{r})$ represents the real valued amplitude of the scattered object field and $(\bar{\nu}+\nu_b)$ represents the temporal frequency of scattered object field.

Similarly, the instantaneous value of the reference field at the virtual detector can be expressed as

$$\mathcal{U}_{reference}(\boldsymbol{r},t) = A_{reference}(\boldsymbol{r})\mathcal{R}_{diffuse}(\boldsymbol{r}) \exp\left(-i\left(\bar{\nu}t + 2\pi\xi_0 x\right)\right) \quad (3\text{-}2)$$

$A_{reference}(\boldsymbol{r})$ represents the real valued amplitude of the reference field and $\bar{\nu}$ represents the temporal frequency of reference field. An additional spatial carrier $2\pi\xi_0 x$ is introduced in the reference beam to help isolate the hologram and twin terms as will be discussed later.

Following the same procedure as in Equation the expression for the instantaneous irradiance detected by the camera is given by,

$$i_{\text{cam}}(\boldsymbol{x},t) = \begin{Bmatrix} \left|A_{object}(\boldsymbol{x})\mathcal{R}_{diffuse}(\boldsymbol{x}) \otimes h_{cam}(\boldsymbol{x})\right|^2 + \left|A_{reference}(\boldsymbol{x})\mathcal{R}_{diffuse}(\boldsymbol{x}) \otimes h_{cam}(\boldsymbol{x})\right|^2 \\ + \exp\left(i\left(v_b t + 2\pi\xi_0 x - \phi_{obj}(\boldsymbol{r})\right)\right) \times \left(A_{object}(\boldsymbol{x})\mathcal{R}_{\text{diffuse}}(\boldsymbol{x}) \otimes h_{\text{cam}}(\boldsymbol{x})\right) \times \text{conj}\left(A_{reference}(\boldsymbol{x})\mathcal{R}_{diffuse}(\boldsymbol{x}) \otimes h_{cam}(\boldsymbol{x})\right) \\ + \exp\left(-i\left(v_b t + 2\pi\xi_0 x - \phi_{obj}(\boldsymbol{r})\right)\right) \times \left(A_{reference}(\boldsymbol{x})\mathcal{R}_{diffuse}(\boldsymbol{x}) \otimes h_{cam}(\boldsymbol{x})\right) \times \text{conj}\left(A_{object}(\boldsymbol{x})\mathcal{R}_{diffuse}(\boldsymbol{x}) \otimes h_{cam}(\boldsymbol{x})\right) \end{Bmatrix} \quad (3\text{-}3)$$

It is evident from the above expression that the hologram term has a spatial and temporal carrier (frequency ξ_0 and ν_b respectively) that is distinct from the other terms. This property forms the basis

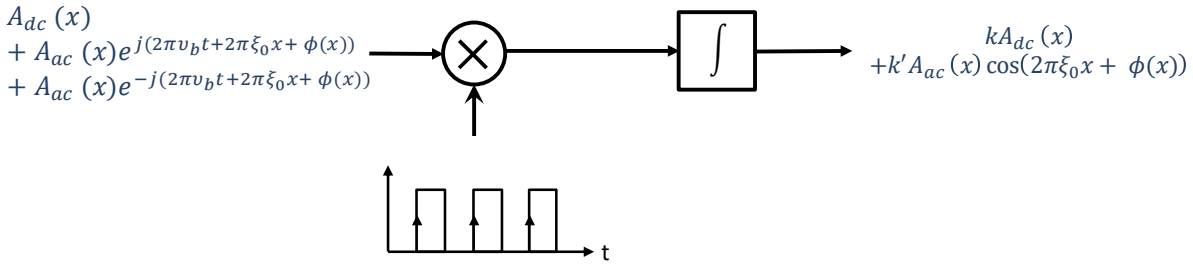

Figure 3-1: Spatio-temporal holography.

of our demodulation stratgey for recovering the hologram. Flutter shutter cameras support repeated strobing of the detector integration within a single exposure, using an external trigger signal. This feature is used to synchronously demodulate the detected irradiance using a square waveform with

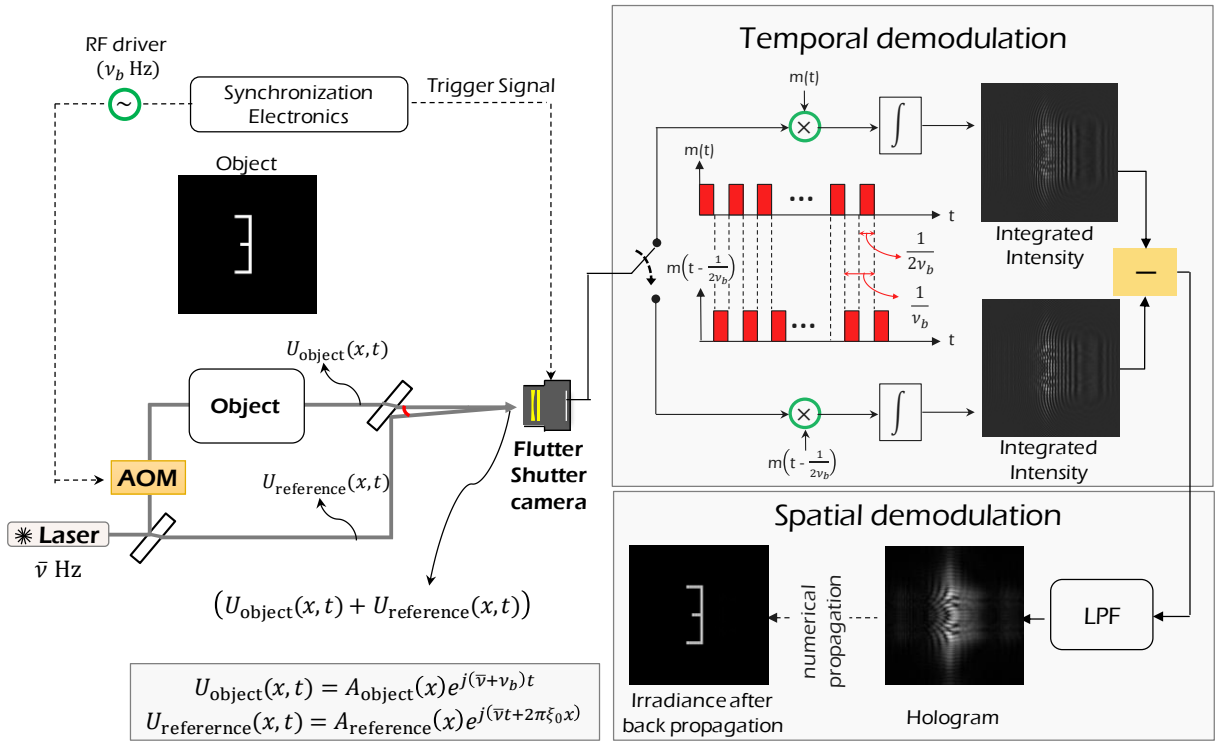

Figure 3-2: Spatio-temporal holography workflow.

temporal frequency ν_b. ference image thus obtained can then be spatially demodulated and low pass filtered to yield the hologram term.

Figure 3-1 illustrates the result of demodulation using a square waveform. The demodulated output can be seen to contain the zeroth order term and the real part of the hologram. The zeroth order term is eliminated by subtracting images recorded using out-of-phase demodulation waveforms or by capturing an image without fluttering the shutter, as shown in the workflow in Figure 3-2. Due to the presence of a carrier term $2\pi\xi_0 x$, the fourier transform of the subtrated image would have the hologram term and the twin term spatially separated (*analogous to off-axis holography*). And hence the name spatio-temporal holography for the approach.

3.2 Indirect imaging using flutter shutter camera

The experimental details are illustrated in Figure 3-3. A collimated laser source (*Vortran Stradus 532 nm, 40 mW, Ø1 mm*) output is split into the reference and the object beams using a non-polarizing cube beam splitter. A frequency shift of 10 *KHz* is introduced in the object beam by passing it through a cascade of two Acousto-optic modulators (*Intraaction AOM-802AF1*). Both the object beam and the reference beam are expanded using a 5X beam expander. The object beam is directed towards a mirror (*Thorlabs BB1-E01*) which acts as a virtual source by the hidden object. The hidden object in this experiment is a reflective USAF target (*Edmund Optics #38-257*) placed between the virtual source and virtual detector. The choice of mirror as virtual source was made to improve the light throughput as this method cannot deal with large power mismatch. The hidden object was placed about 0.8 meters behind the virtual detector.

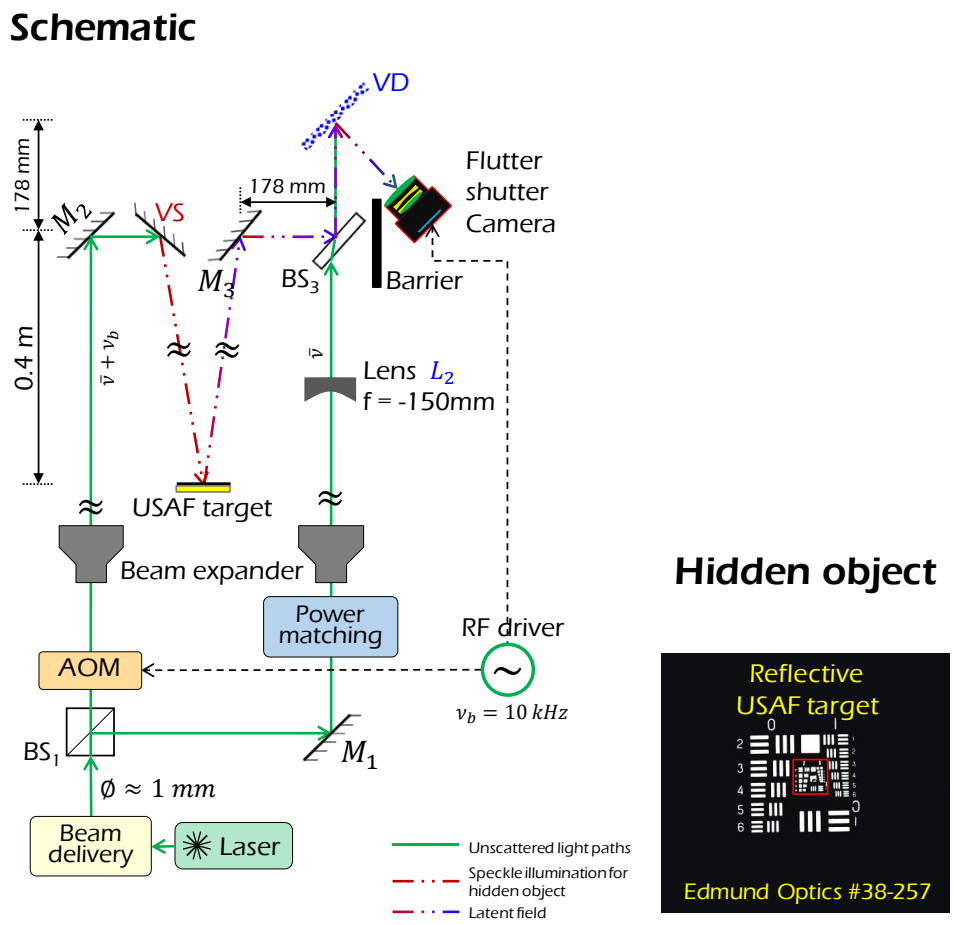

Figure 3-3: Spatio-temporal holography schematic.

The expanded beam in the reference arm is directed through a 150-mm bi-concave diverging lens to creates a virtual focus at the axial location of the object plane. The reference field and the latent field are recombined using a plate beam splitter and are directed towards a painted dry wall, which acts as a virtual detector. Diffraction limited imaging optics (*Thorlabs MVL 50TM23*) relays the irradiance pattern at the virtual detector towards the flutter-shutter camera (*PointGrey FL3-GE-28S4M*). The image of the object is reconstructed by computing the magnitude of the Fourier transform of the latent hologram. It can be observed from Figure 3-3 that the hidden object can be

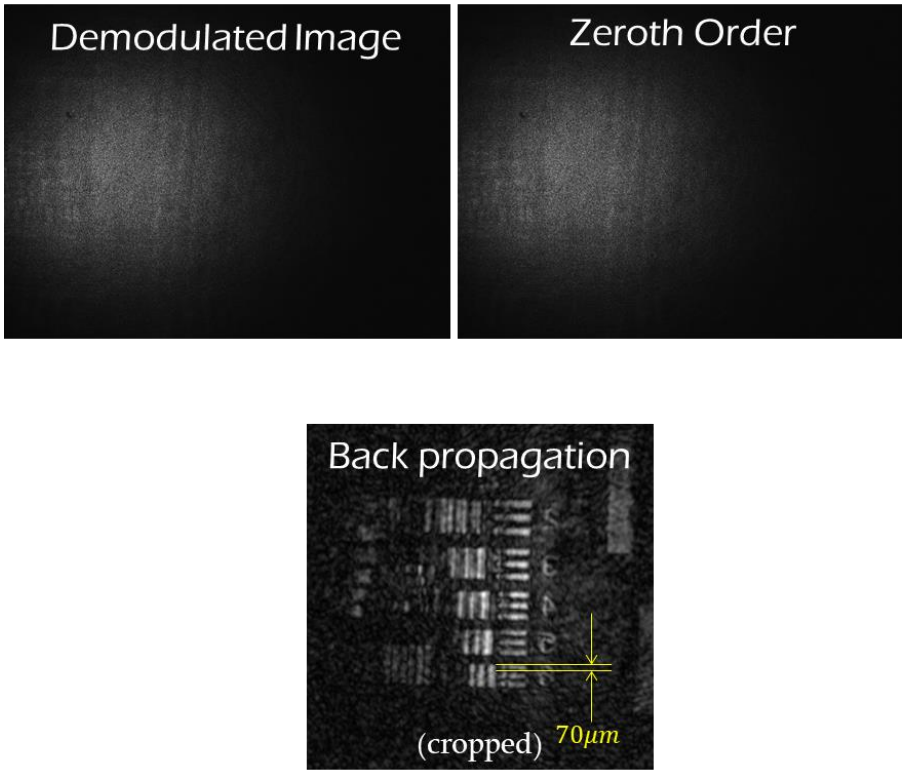

Figure 3-4: Spatio-temporal holography results.

reconstructed with a resolution of the order of 70 µm at 0.8 meters standoff using this approach. The flutter-shutter camera (*with a pixel pitch of 3.69 µm*) can thus sense very fine spatial frequencies in the latent hologram compared to the lock-in camera (with a pixel pitch of 39.6 µm) and thus significantly improving the spatial resolution.

3.3 Performance of spatio-temporal holographic approach using flutter shutter camera

The FOV and the resolution of spatio-temporal holography using flutter shutter camera can be estimated following a similar approach taken in Section 2.6.1. The Flutter-shutter camera used has a pixel pitch of 3.69 µm and dimensions of 7.1 mm × 5.3 mm. The resolution on target and the FOV are given in the table below. It can be observed by comparing the two tables that the Flutter

shutter camera-based approach has 10 times more FOV compared to the lock-in camera based approach with a slight loss in the resolution on target.

Wavelength $= 0.532\mu m$

Parameter	$Z_r = 1m$
Inclination of reference β_r	1°
Magnification, M	0.51
Size of hologram $S\ mm \times S\ mm$	14.2×14.2
Minimum inter sample(ISS) spacing at VD $\sqrt{A_{pixel}}$	$7.621\ \mu m$
$\beta_{\min}$, $\beta_{\max}$	0° , -1°
Maximum size of hidden object $X_{\max} - X_{\min}$	$17.4\ mm$
Minimum achievable resolution on target	$37.46\ \mu m$

Figure 3-5: FOV and resolution of Flutter shutter camera.

In the spatio-temporal holography experiments in reflection mode, 70 µm bars occupied ~3 pixels resulting in an effective resolution of ~24 µm (*A magnification of 0.5 is assumed in the analysis which is closer to 0.4 magnification used in the experiments*).

3.3.1 Signal to background limitations

To understand signal to background limitations of the Flutter-shutter camera, an approach similar to reference [24] is adopted. Consider the interference of a weak signal with a photon flux of 1

photo-electron per pixel, with a strong reference signal of photon flux N = $\frac{\text{full well capacity}}{2}$ within the integration time of say 1s.

For the Flutter-shutter camera, the full well capacity is 11586 photoelectrons [41]. We neglect the quantum efficiency of the sensor for this discussion as it will be a constant factor. So, consider a reference signal with photon flux of ~ 5000 photoelectrons. Assuming the signal is shot-noise limited, the total number of photoelectrons due to shot-noise becomes $\sqrt{N}$. The hologram term also has a strength of $\sqrt{N \times 1}$ photoelectrons. Thus, the SNR becomes ~1 in this case. So, for an SNR of 1, the maximum power mismatch tolerable without saturating the sensor is about approximately 0.5×10^4. As the full well capacity of the sensor is wasted in recording large unmodulated reference signal, the maximum power mismatch that can be tolerated in this case is only 0.5×10^4 before the sensor starts to saturate.

Now, consider the case of a lock-in camera. Due to the presence of an offset compression circuitry to suppress the unmodulated signal and increase the full well capacity, the lock-in camera has a very low responsivity to unmodulated signal compared to the modulated signal. At 532 nm, the responsivity of lock-in camera to modulated signal is $920000\ \text{DU/J/m}^2$, whereas the responsivity for unmodulated signal is $160\ \text{DU/J/m}^2$ [31]. DU here represents the digital unit which is the output counts. The responsivities differ by a factor of 5750. So, the maximum power mismatch tolerable without saturating the sensor in the case of a lock-in camera is about order 10^4 times more than the Flutter shutter camera.

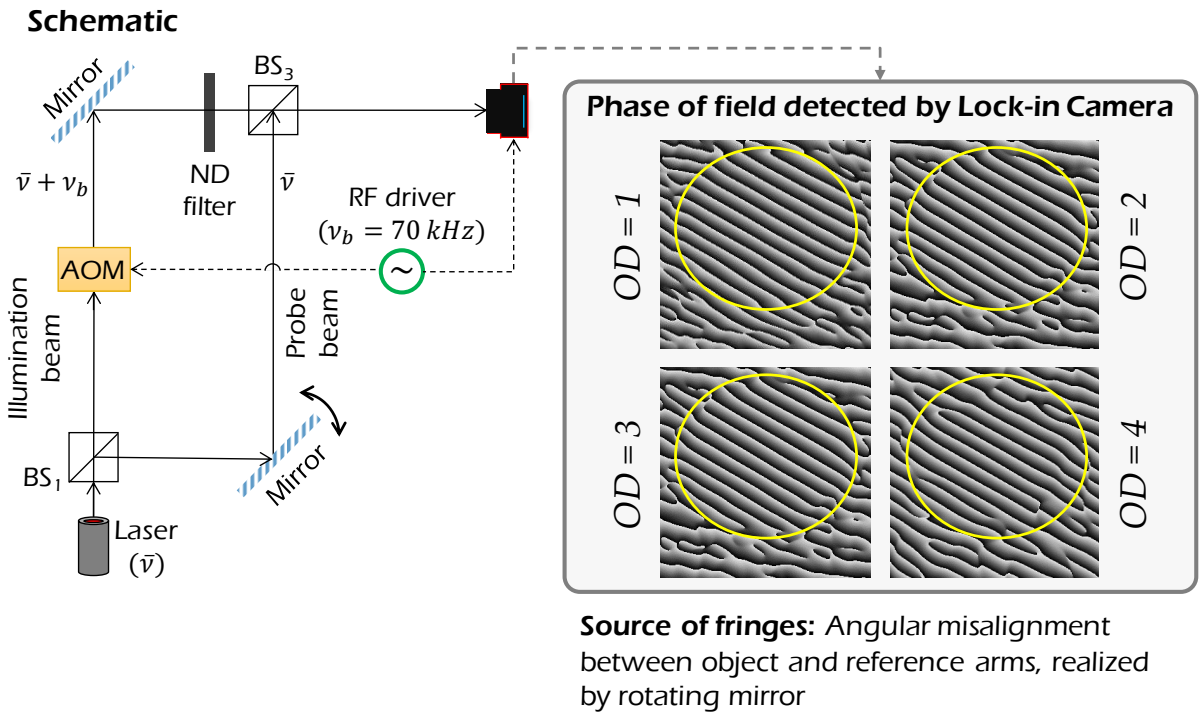

Figure 3-6: Lock-in detection with low signal to background ratios.

An experimental setup to verify the working of lock-in camera under large signal to background conditions was performed as illustrated in Figure 3-6. A collimated laser source (*532 nm, 20 mW, Ø1 mm*) output is split into the reference and the object beams using a non-polarizing cube beam splitter. A frequency shift of 70 KHz is introduced in the object beam by passing it through a cascade of two Acousto-optic modulators (*Intraaction AOM-802AF1*). Deliberate angular misalignment has been introduced between the two arms to visualize interference fringes. ND filter of varying optical densities are used to introduce the power mismatch between the beams. Fringes can be observed even at OD4 mismatch.

3.3.2 Comparison with off-axis holography and phase shifting holography

The approach presented requires at least one less measurement that a traditional phase-shifting holographic approach. Hence, with fewer measurements that phase-shifting holographic approach, the hologram of the hidden object can be recovered.

When compared to the off-axis digital holographic approach, this approach has a better utilization of spatial bandwidth. In off-axis holography, all the three terms of interference are recorded in a single frame and it is directly used to reconstruct the hologram. The autocorrelation terms occupy a bandwidth of 2B, leaving an effective bandwidth of B for the hologram terms. In this approach, by capturing the zeroth order term independently, the effective bandwidth available for the hologram terms is doubled.

3.4 Summary

The approach presented in this chapter has a good spatial resolution than heterodyne RDH using lock-in camera and good temporal resolution compared to Phase-shifting RDH. The presented method also has a good bandwidth utilization in recording object's hologram compared to off-axis holography. Albeit, it cannot deal with power mismatch between the latent field and the reference field. This limits its use in practical scenarios with very high-power mismatch.

Chapter 4

DETECTING MOTION AROUND A CORNER

With heterodyne interferometry using lock in camera, the hologram of the hidden object is obtained in a single shot with the exposure times of the order of few milli-seconds. This fact enables the possibility of detecting and characterizing motion profiles of around the corner. In this chapter, we explore the possibility of detecting rapidly varying and slowly varying motion of object around a corner using doppler shifts and speckle correlations respectively. The following sections describe the methods and experiments employed to discern motion of objects around a corner.

4.1 Discerning rapidly varying motion using doppler shifts

It is a well-known phenomenon that light bouncing off an object/mirror moving with uniform velocity undergoes a doppler shift in frequency. It manifests as a constant frequency shift of the light reflected off the object. Similarly, more complex motion profiles of the object introduce complex temporal frequency shifts in the reflected light.

For example, consider an object exhibiting simple harmonic motion at a frequency ν_s and amplitude z_s. A normally incident beam illuminating this vibrating object undergoes a phase shift that can be expressed as:

$$\phi(t) = 4\pi z_s \sin(2\pi \nu_s t) \tag{4-1}$$

The field scattered off the object can be expressed as

$$\mathcal{U}_{object}(\boldsymbol{x}, t) = \mathrm{A}(x)\exp(i4\pi z_s \sin(2\pi \nu_s t)) \tag{4-2}$$

Equation (4-2) can be expanded using Jacobi-Anger expansion, to obtain,

$$\mathcal{U}_{object}(\boldsymbol{x}, t) = \mathrm{A}(x) \sum_{m} J_m(4\pi z_s) \exp(i2\pi m \nu_s t) \tag{4-3}$$

It can be seen from Equation (4-3) that the scattered field is a summation of sideband frequencies. Thus, by estimating the frequency spectrum of the light reflected off the object, the type of motion it underwent can be deduced. The frequency spectrum of scattered light can be estimated using heterodyne interferometry. Under the condition that the angular separation between the latent field and the reference field is small and within the isoplanatic angle of the virtual detector the hologram of the object at these frequency bands can also be estimated which can help in detecting vibration modes of the object as is done in holographic vibrometry [38].

The proof-of-principle experiment to discern rapid motion of objects around a corner is like the heterodyne RDH setup and is illustrated in Figure 4-1. The output beam from a collimated laser source (*Vortran Stradus 532 nm, 40 mW, Ø1 mm*) is split into the reference and the object beams. A frequency shift of 10 KHz is introduced in the object beam by passing it through a cascade of two Acousto-optic modulators (*Intraaction AOM-802AF1*). Both the object beam and the reference beam are expanded using a 5X beam expander. The object beam is directed towards a mirror (*Thorlabs BB2-05*) which acts as a virtual source by the hidden object. The hidden object in this experiment is a cutout of character '7' mounted attached to a loud speaker placed between the virtual source and virtual detector. The loud speaker was set to play a 5 KHz tone. The choice of mirror as virtual source was made to improve the light throughput at the sideband frequencies. The hidden object was placed about 0.4 meters behind the virtual detector.

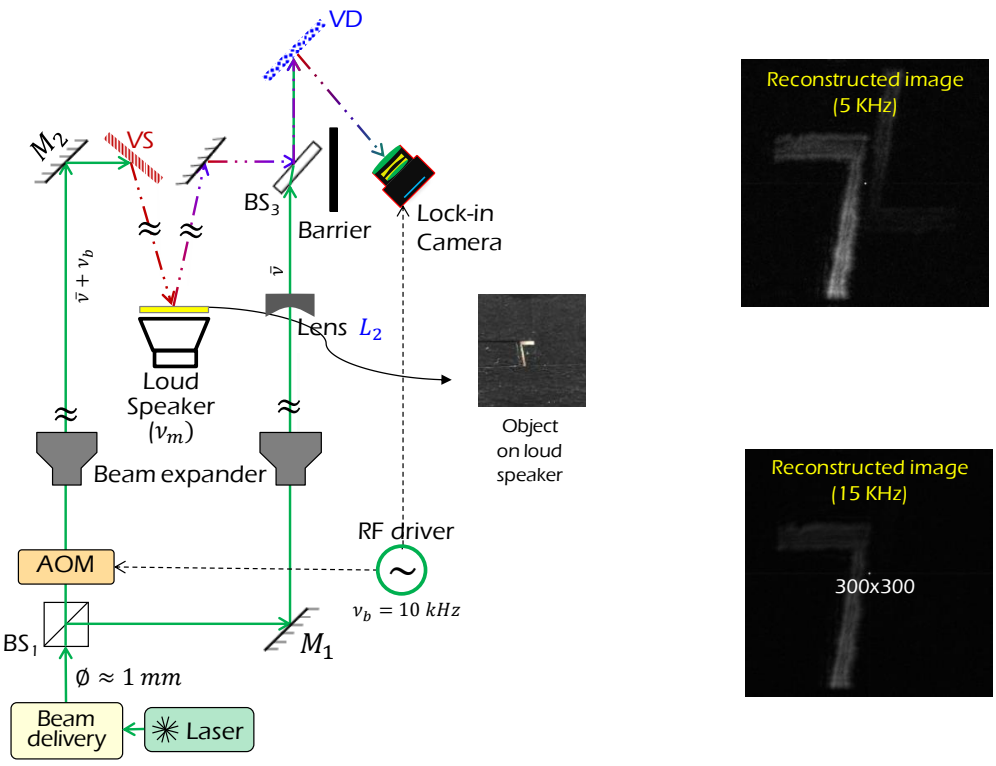

Figure 4-1: Recovering rapid motion around a corner schematic and results.

The expanded beam in the reference arm is directed through a 150-mm bi-concave diverging lens to creates a virtual focus at the axial location of the object plane. The reference field and the latent field are recombined using a plate beam splitter and are directed towards a painted drywall panel, which acts as a virtual detector. The lock-in camera outputs an in-phase and quadrature image by demodulating the irradiance different sideband frequencies (5 *KHz*, 15 *KHz*). The image of the object is reconstructed by computing the magnitude of the Fourier transform of the averaged latent hologram. As illustrated in Figure 4-1, object reconstructions can be observed at 5 *KHz* and 15 *KHz* which happen to be the +1 and -1 order sidebands around the heterodyne frequency of 10 KHz. These signals are due to the vibrating object. This experiment demonstrates that rapidly varying object motion around a corner can be discerned using heterodyne RDH. This method can

be extended by using a single pixel detector (*with a lock-in detector*) to give the temporal resolution to detect the frequency profile of the latent field and using lock-in camera to lock-in to one frequency at a time and recover a hologram at that frequency.

4.2 Discerning slowly varying motion around a corner using speckle correlations

Adapting ideas from line of sight motion estimation techniques such as speckle photography and electronic speckle pattern interferometry, slowly varying motion of objects around corner can be estimated. Rigid body motion of the hidden object results in a change in speckle pattern observed at the Virtual Detector. For small rotations and in-plane translations, the speckle pattern observed at the virtual detector tracks the object motion [37]. This results in a highly correlated and shifted copy of the speckle pattern observed at Virtual Detector, before and after object displacement. Computing the Fourier modulus of the difference of the speckle images yields linear fringes encoding speckle motion. The direction of motion is inferred from the orientation of the fringes. The magnitude of motion is inferred from the periodicity of the fringes.

Continuous tracking of the moving object is possible by rapidly acquiring the time-varying speckle patterns at VD and subsequent processing of the differential motion between neighboring frames. In addition to recovering latent motion information, an intensity image of the hidden object can also be extracted from the recorded speckle patterns at VD by adapting techniques from imaging correlography [20]. It relies on the notion that the indirectly illuminated hidden object may be viewed as a collection of secondary point-sources that interfere pairwise to produce Young's fringes at the Virtual Detector. An estimate of the autocorrelation of the object intensity is obtained from the Fourier modulus of the spatial pattern observed at VD. An image of the hidden object can be recovered from the estimated autocorrelation using phase retrieval techniques.

The experimental details are illustrated in Figure 4-2. A collimated laser source (*Vortran Stradus 532 nm, 40 mW, Ø1 mm)* output is expanded using a 10X beam expander (*Edmund Optics Tech spec series + Asphericon 2X*) and focused on to the Virtual source using a 500-mm converging lens. Focused spot illumination of the virtual source ensures that the speckle pattern illuminating the hidden volume is comprised of large blobs of homogenous amplitude. In the experiment hidden object is a US quarter (as shown in the Figure 4-2) placed behind two painted dry wall panels acting as virtual source and virtual detector. The hidden object is placed 0.41 meters from the virtual source and 0.56 meters behind the virtual detector. The irradiance distribution on the virtual detector is imaged on to a camera (*PointGrey FL3-GE-28S4M*) using a machine vision lens (*Thorlabs MVL 50TM23*). The object is mounted on a stepper-motor actuated translation stage (*Zaber T-LA13A-S*) that moves in increments of 10µm between frames.

In the proof of principle experiment, the images of the speckle pattern on the virtual detector are captured using a camera at discrete steps of motion of the object. From the stack of these images, a reference image is chosen with respect to which the shifts in the subsequent speckle patterns are measured. By taking the Fourier modulus of the difference of the speckle images, fringes corresponding to the speckle motion are obtained as illustrated in Figure 4-3. The shifts between the speckle patterns is encoded in the period of the fringes. The exact shift observed between the captured images depends also on the pose of the object and its distance from the virtual source and virtual detector. General expressions for speckle motion as the object undergoes rigid body motion are presented in [38].

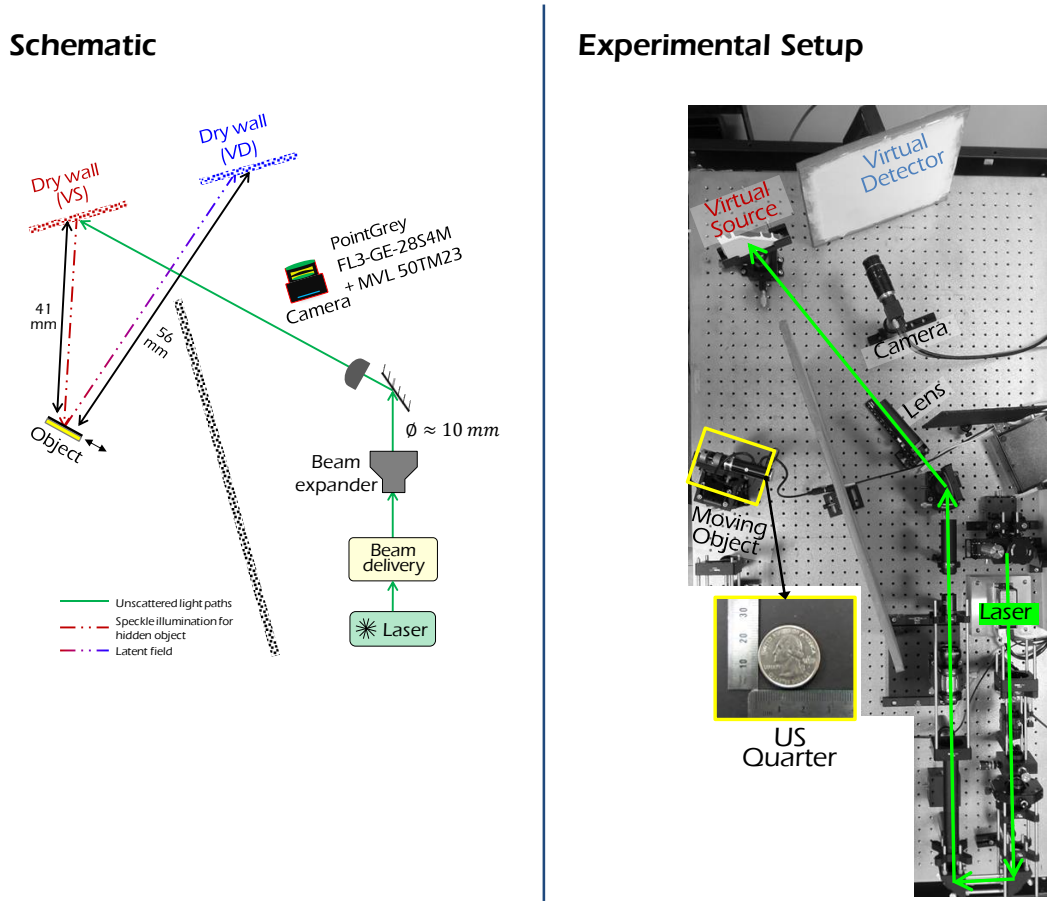

Figure 4-2: Discerning slowly varying motion around a corner.

Hence, the actual shift in the pattern observed will be a scaled version of the actual motion underwent by the body. The relationship between the actual motion of the object and the observed

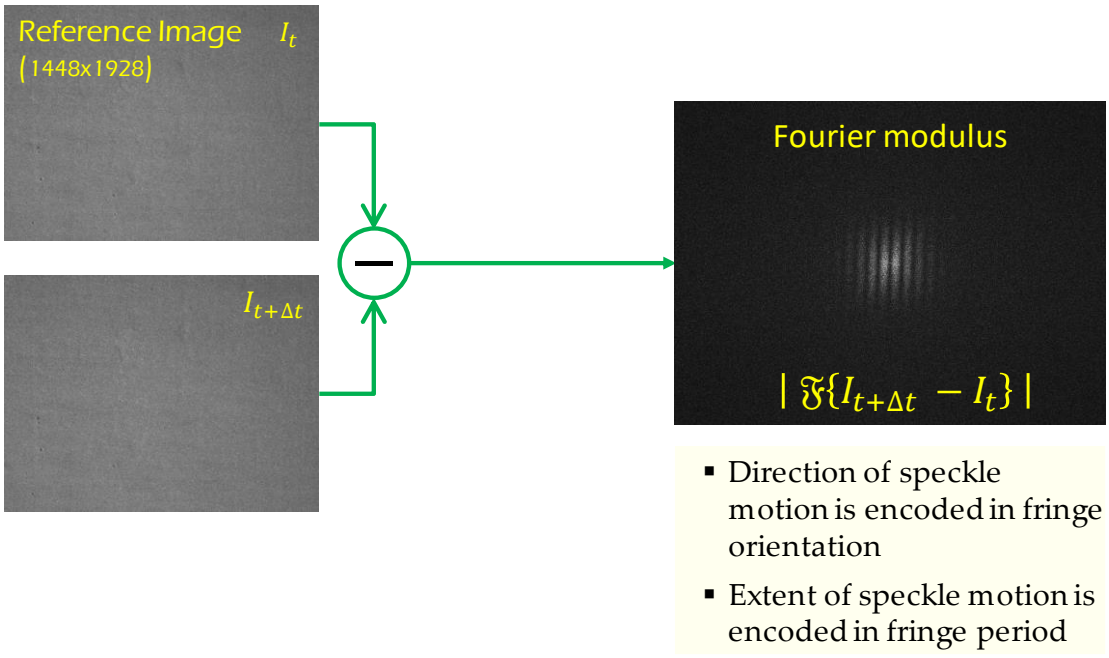

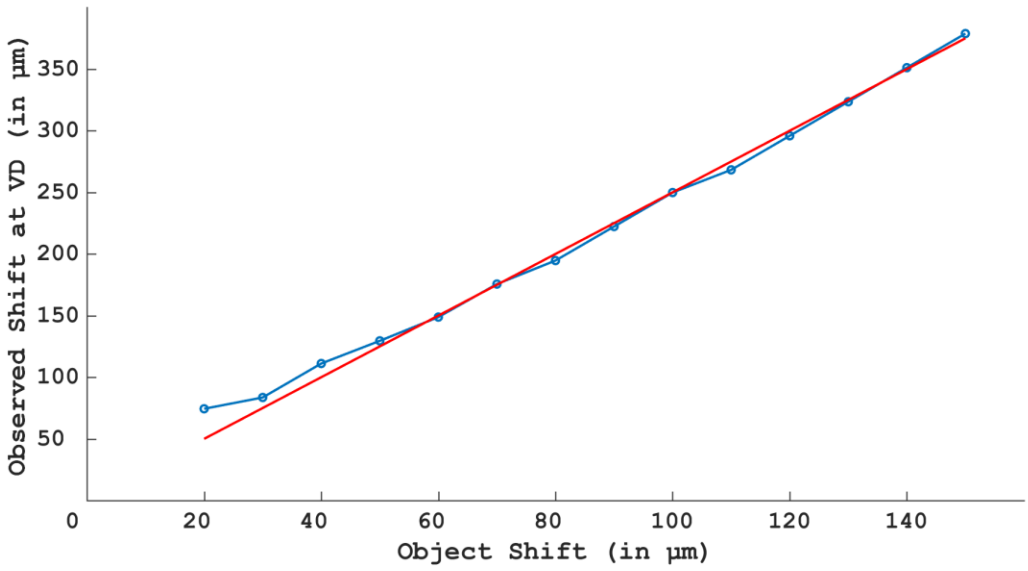

Figure 4-3: Motion estimation from the captured frames.

shifts in the speckle pattern is verified to be linear as seen in Figure 4-3.

The autocorrelation of the hidden object can also be extracted from the captured images by adapting techniques from imaging correlography [20]. The indirectly illuminated hidden object can be thought of as a collection of secondary point sources that self-interfere to produce fringes at the virtual detector. The estimate of the autocorrelation of the illuminated object is obtained by computing the Fourier transform of the detected intensity pattern at virtual detector. The image of the hidden object is obtained from the estimated autocorrelation using phase retrieval techniques.

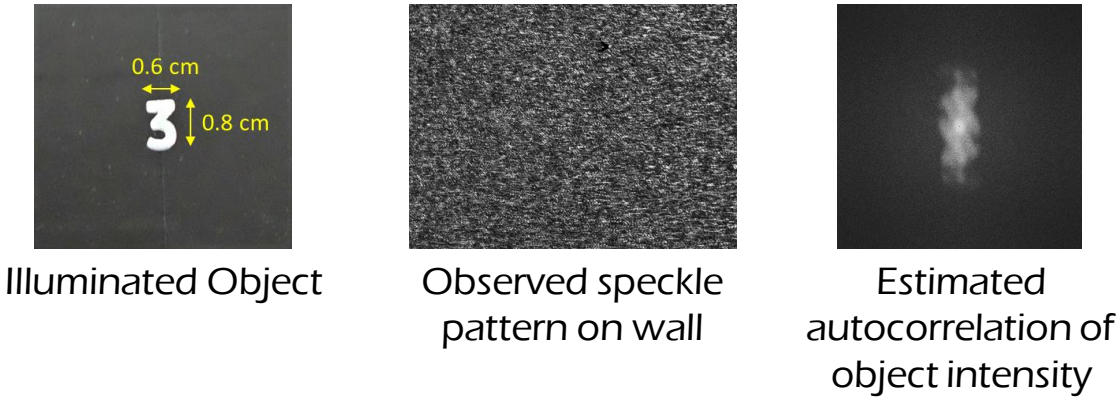

Figure 4-4: Estimation of the object's autocorrelation around a corner.

In this experiment, a retro-reflective sticker in the shape of the number "3" is used as a hidden object placed behind a silver foil (*Virtual Source*) and a drywall panel (*virtual detector*). A retro-reflective object and the silver foil virtual source are chosen such that high contrast speckle pattern can be observed at the virtual detector. The observed speckle pattern and the estimated auto-correlation of the object intensity estimated from one of the captured frames are shown in Figure 4-4. Thus, these experiments establish that using speckle shifts, both the motion of the object and its incoherent image can be detected around a corner.

When there is significant motion within each frame, the speckle details are lost due to motion blur. This problem was addressed in line of sight based methods by strobing the illumination to obtain motion trajectories [39]. With the availability of advanced detectors such as the flutter-shutter camera, the strobing can be done on the detection side with varying duty cycles to obtain the motion trajectories of objects. Figure 4-5 illustrates a proof-of-principle experiment performed in the line of sight imaging scenario using the flutter shutter camera. The object was a dime moving on a stepper-motor actuated translation stage (*Zaber T-LA13A-S*) at a constant velocity of 2 mm/s. As the velocity is high enough, motion blur is severe and would require high-speed cameras to resolve the speckle detail. In the experiment, the object was illuminated by a coherent laser beam and the scattered speckle pattern is detected using a flutter shutter camera operating at 40 Hz and capturing 30 flutters per frame. Upon cross correlating the fluttered frame with the reference frame, the motion trajectory of the object can be observed.

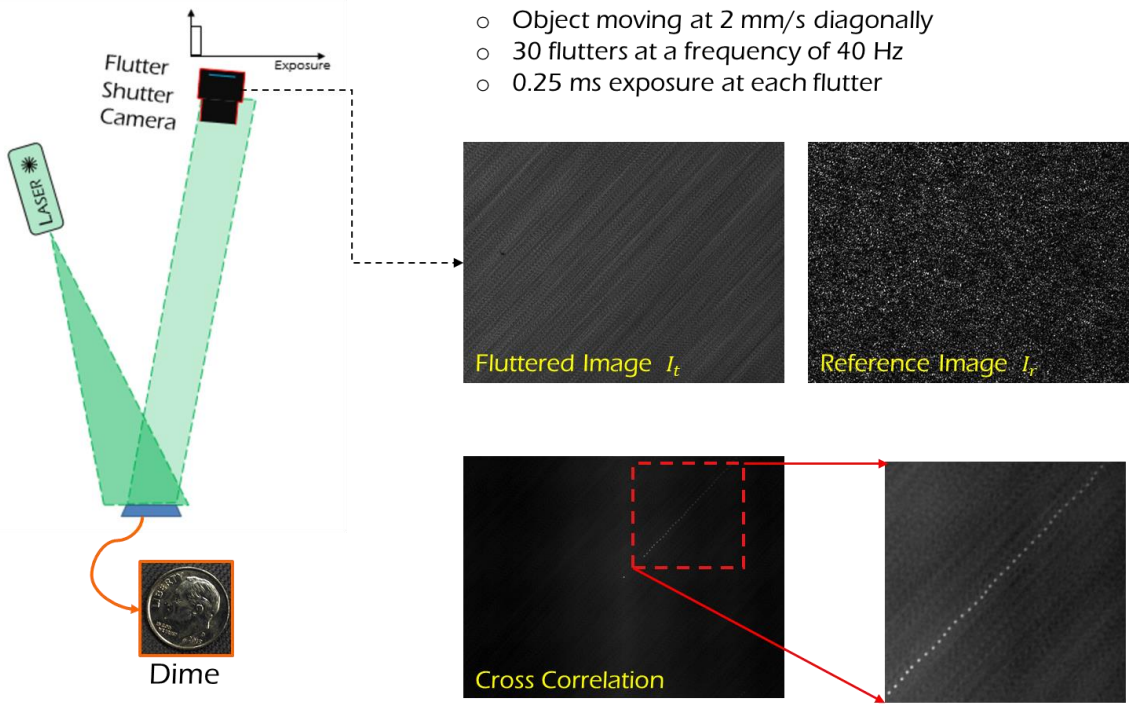

Figure 4-5: Detecting motion trajectories in the line of sight using flutter shutter camera.

4.3 Summary

Experimental validation of estimating rapidly varying and slowly varying motion of objects around a corner using doppler shifts and speckle correlations is discussed in this chapter. Motion type and motion trajectories of objects can be estimated using the methods discussed in this chapter.

Chapter 5

CONCLUSION

Advancements in detection technologies have enabled the adaptation of heterodyne interferometry techniques to obtain full field information of an object hidden around a corner. Use of a strong reference beam to amplify the weak return from the object has been experimentally validated and a hologram of the hidden object is obtained. The methods discussed in this thesis can be extended for use in applications beyond indirect imaging. The unique features offered by the lock-in camera can have potential applications in line of sight imaging to obtain 3D images of objects even under bright background conditions. Heterodyne interferometry itself can be extended towards multiple wavelength (or) super heterodyne interferometry-based imaging modalities to look around corners.

Appendix

Lock-in camera demodulation:

Lock-in camera demodulates the temporally oscillating irradiance using a bipolar demodulation waveform that approximates a sinusoid as shown in Figure 1-5. Let the irradiance of the interference be given by:

$$I(\boldsymbol{x},t) = \begin{array}{c} |A_{\text{reference}}(\boldsymbol{x})|^2 + \left|A_{\text{Object}}(\boldsymbol{x})\right|^2 + \\ A_{\text{reference}}(\boldsymbol{x})A_{\text{object}}(\boldsymbol{x})\exp\left(-i(2\pi\nu_b t + \emptyset)\right) \\ + A_{\text{reference}}(\boldsymbol{x})A_{\text{object}}(\boldsymbol{x})\exp\left(i(2\pi\nu_b t + \emptyset)\right) \end{array} \quad (0\text{-}1)$$

Where, $A_{\text{reference}}(\boldsymbol{x})$ and $A_{\text{object}}(\boldsymbol{x})$ are the real valued ampitude of the object and reference beam respectively, $\emptyset$ is the relative phase of the object with respect to reference and ν_b is the beat frequency. The above equation can be expressed as,

$$I(\boldsymbol{x},t) = \begin{array}{c} |A_{\text{reference}}(\boldsymbol{x})|^2 + \left|A_{\text{Object}}(\boldsymbol{x})\right|^2 + \\ 2A_{\text{reference}}(\boldsymbol{x})A_{\text{object}}(\boldsymbol{x})\cos(2\pi\nu_b t + \emptyset) \end{array} \quad (0\text{-}2)$$

The in-phase component of the lock-in camera can be expressed as,

$$I_{in-phase}(\boldsymbol{x}) = \begin{array}{c} \int_0^{\frac{1}{4\nu_b}} \begin{pmatrix} |A_{\text{reference}}(\boldsymbol{x})|^2 + \left|A_{\text{Object}}(\boldsymbol{x})\right|^2 + \\ 2A_{\text{reference}}(\boldsymbol{x})A_{\text{object}}(\boldsymbol{x})\cos(2\pi\nu_b t + \emptyset) \end{pmatrix} dt \\ - \\ \int_{\frac{1}{2\nu_b}}^{\frac{3}{4\nu_b}} \begin{pmatrix} |A_{\text{reference}}(\boldsymbol{x})|^2 + \left|A_{\text{Object}}(\boldsymbol{x})\right|^2 + \\ 2A_{\text{reference}}(\boldsymbol{x})A_{\text{object}}(\boldsymbol{x})\cos(2\pi\nu_b t + \emptyset) \end{pmatrix} dt \end{array} \quad (0\text{-}3)$$

Upon simplifying, the above equation becomes,

$$I_{in-phase}(\boldsymbol{x}) = \frac{2A_{\text{reference}}(\boldsymbol{x})A_{\text{object}}(\boldsymbol{x})}{\pi\nu_b}\cos(\emptyset) \tag{0-4}$$

Similarly, the quadrature image can be expressed as,

$$I_{quadrature}(\boldsymbol{x}) = \int_{\frac{1}{4\nu_b}}^{\frac{1}{2\nu_b}} \begin{pmatrix} |A_{\text{reference}}(\boldsymbol{x})|^2 + |A_{\text{Object}}(\boldsymbol{x})|^2 + \\ 2A_{\text{reference}}(\boldsymbol{x})A_{\text{object}}(\boldsymbol{x})\cos(2\pi\nu_b t + \emptyset) \end{pmatrix} dt - \int_{\frac{3}{4\nu_b}}^{\frac{1}{\nu_b}} \begin{pmatrix} |A_{\text{reference}}(\boldsymbol{x})|^2 + |A_{\text{Object}}(\boldsymbol{x})|^2 + \\ 2A_{\text{reference}}(\boldsymbol{x})A_{\text{object}}(\boldsymbol{x})\cos(2\pi\nu_b t + \emptyset) \end{pmatrix} dt \tag{0-5}$$

Simplifying,

$$I_{quadrature}(\boldsymbol{x}) = \frac{2A_{\text{reference}}(\boldsymbol{x})A_{\text{object}}(\boldsymbol{x})}{\pi\nu_b}\sin(\emptyset) \tag{0-6}$$

REFERENCES

1. J. W. Goodman, Introduction to Fourier Optics, McGraw-Hill, New York, NY, USA, 2ed edition, 1996.

2. Myung K.Kim, Digital Holographic Microscopy

3. Emmett N. Leith and Juris Upatnieks, "Wavefront Reconstruction with Diffused Illumination and Three-Dimensional Objects*," J. Opt. Soc. Am. 54, 1295-1301 (1964).

4. A. Velten, T. Willwacher, O. Gupta, A. Veeraraghavan, M. G. Bawendi, and R. Raskar, "Recovering ThreeDimensional Shape around a Corner using Ultra-Fast Time-of-Flight Imaging." Nature Communications, March 2012, http://dx.doi.org/10.1038/ncomms1747

5. J M. O'Toole, F. Heide, D. Lindell, K. Zang, S. Diamond, G. Wetzstein, "Reconstructing Transient Images from Single-Photon Sensors", IEEE Int. Conference on Computer Vision and Pattern Recognition (CVPR), 2017.

6. E. Leith, H. Chen, Y. Chen, D. Dilworth, J. Lopez, R. Masri, J. Rudd, and J. Valdmanis, "Electronic holography and speckle methods for imaging through tissue using femtosecond gated pulses," Appl. Opt. 30, 4204-4210 (1991).

7. Jeremy C. Hebden, Robert A. Kruger, and K. S. Wong, "Time resolved imaging through a highly scattering medium," Appl. Opt. 30, 788-794 (1991).

8. I. Freund, "Looking through walls and around corners," Phys. A 168, 49–65 (1990).

9. O. Katz, P. Heidmann, M. Fink, and S. Gigan, "Non-invasive singleshot imaging through scattering layers and around corners via speckle correlations," Nat. Photonics 8, 784–790 (2014).

10. X. Xu, H. Liu, and L. V. Wang, "Time-reversed ultrasonically encoded optical focusing into scattering media," Nat Photon, vol. 5, no. 3, pp. 154–157, Mar. 2011.

11. J. W. Goodman and W. H. Huntley, Jr., D. W. Jackson and M. Lehmann, "Wavefront-reconstruction imaging through random media," Appl. Phys. Lett. 8, 311–313 (1966).

12. H. Kogelnik and K. S. Pennington, "Holographic imaging through a random medium," J. Opt. Soc. Am. 58, 273–274 (1968).

13. Alok Kumar Singh, Dinesh N. Naik, Giancarlo Pedrini, Mitsuo Takeda, and Wolfgang Osten, "Looking through a diffuser and around an opaque surface: A holographic approach," Opt. Express 22, 7694-7701 (2014).

14. Michael J. Purcell, Manish Kumar, Stephen C. Rand, and Vasudevan Lakshminarayanan, "Holographic imaging through a scattering medium by diffuser-aided statistical averaging," J. Opt. Soc. Am. A33, 1291-1297 (2016).

15. P. Rangarajan and M. P. Christensen, "Imaging hidden objects by transforming scattering surfaces into computational holographic sensors," in *Imaging and Applied Optics 2016*, OSA Technical Digest (online) (Optical Society of America, 2016), paper CTh4B.4.

16. E. Arons and D. Dilworth, "Analysis of Fourier synthesis holography for imaging through scattering materials," Appl. Opt. 34, 1841-1847 (1995).

17. E. Leith, C. Chen, H. Chen, Y. Chen, D. Dilworth, J. Lopez, J. Rudd, P.-C. Sun, J. Valdmanis, and G. Vossler, "Imaging through scattering media with holography," J. Opt. Soc. Am. A9, 1148-1153 (1992).

18. Eitan Edrei and Giuliano Scarcelli, "Optical imaging through dynamic turbid media using the Fourier-domain shower-curtain effect," Optica3, 71-74 (2016).

19. A. Viswanath, P. Rangarajan, D. MacFarlane, and M. P. Christensen, "Indirect Imaging Using Correlography," in *Imaging and Applied Optics 2018 (3D, AO, AIO, COSI, DH, IS, LACSEA, LS&C, MATH, pcAOP)*, OSA Technical Digest (Optical Society of America, 2018), paper CM2E.3.

20. J. Fienup and P. Idell, "Imaging Correlography With Sparse Arrays of Detectors", Optical Engineering, vol. 27, no. 9, 1988.

21. Report for Phase 1 of OMNISCIENT, Technical report submitted to DARPA REVEAL: HR0011-16-C-0028.

22. René Dändliker,I Heterodyne Holographic Interferometry, 1980

23. L. Mandel, "Heterodyne Detection of a Weak Light Beam*," J. Opt. Soc. Am. 56, 1200-1206 (1966).

24. Frédéric Verpillat, Fadwa Joud, Michael Atlan, and Michel Gross, "Digital Holography at Shot Noise Level," J. Display Technol. 6, 455-464 (2010).

25. Matsumoto, Hirokazu & Hirai, Akiko. (1999). White-light interferometer using a lamp source and heterodyne detection with acousto-optic modulators. Optics Communications - OPT COMMUN. 170. 217-220. 10.1016/S0030-4018(99)00471-X.

26. Space-based gravitational wave detection with LISA, D A Shaddock, Published 15 May 2008 ,Classical and Quantum Gravity, Volume 25, Number 11.

27. Liu,Yan and Shen,Yuecheng and Ma,Cheng and Shi,Junhui and Wang,Lihong V, Lock-in camera based heterodyne holography for ultrasound-modulated optical tomography inside dynamic scattering media, Applied Physics Letters.

28. Louis C.Philips and James Wagner, “The investigation of the fundamental limits of heterodyne holographic interferometry with the application in imaging laser generated lamb waves”, Technical Report ONR Contract N00014-82K-0741-P04.

29. Goodman JW. Speckle phenomena in optics: theory and applications. Roberts and Company Publishers; 2007.

30. Foix S, Alenya G, Torras C. Lock-in time-of-flight (ToF) cameras: A survey. IEEE Sensors Journal. 2011 Sep;11(9):1917-26.

31. http://www.heliotis.ch/html/lockInCameraC3.htm

32. Real time photon noise limited oct based on pixel level analog signal processing, Stephane BEER.

33. M J. Lavan, G. E. Van Damme, W. K. Cadwallender, "Mach-Zehnder Heterodyne Interferometer," Optical Engineering 15(5), 155464 (1 October 1976).

34. Malacara, Optical Shop Testing, 3rd ed.

35. Freund I, Rosenbluh M, Feng S. Memory effects in propagation of optical waves through disordered media. Physical review letters. 1988 Nov 14;61(20):2328.

36. Raskar, Ramesh & Agrawal, Amit & Tumblin, Jack. (2006). Coded Exposure Photography: Motion Deblurring using Fluttered Shutter. ACM Trans. Graph.. 25. 795-804. 10.1145/1141911.1141957.

37. Pierre Jacquot and Pramod K. Rastogi, "Speckle motions induced by rigid-body movements in free-space geometry: an explicit investigation and extension to new cases," Appl. Opt. 18, 2022-2032 (1979).

38. Verrier, N., Atlan, M. and Gross, M. (2015),” Full Field Holographic Vibrometry at Ultimate Limits, in New Techniques in Digital Holography (ed P. Picart)”, John Wiley & Sons, Inc., Hoboken, NJ, USA. doi: 10.1002/9781119091745. ch7.

39. A. W. Lohmann and G. P. Weigelt, "Speckle methods for the display of motion paths," J. Opt. Soc. Am. 66, 1271-1274 (1976).

40. A. Viswanath, P. Rangarajan, I. Sinharoy, D. MacFarlane, and M. P. Christensen, "Impact of scattering on holographic approaches to recovering latent scene information from scattered light," in Imaging and Applied Optics 2017 (3D, AIO, COSI, IS, MATH, pcAOP), OSA Technical Digest (online) (Optical Society of America, 2017), paper CTu2B.2.

41. https://www.ptgrey.com/support/downloads/10443.